

1 **A Regional CO₂ Observing System Simulation Experiment for the ASCENDS Satellite**
2 **Mission**

3
4 James S. Wang,^{1,2} S. Randolph Kawa,² Janusz Eluszkiewicz,^{3,*} David F. Baker,⁴ Marikate
5 Mountain,³ John Henderson,³ Thomas Nehrkorn,³ and T. Scott Zaccheo³

6
7
8 ¹Universities Space Research Association, Columbia, MD, USA, james.s.wang@nasa.gov

9 ²NASA Goddard Space Flight Center, Greenbelt, MD, USA

10 ³Atmospheric and Environmental Research, Lexington, MA, USA

11 ⁴Cooperative Institute for Research in the Atmosphere, Colorado State University, Fort Collins,
12 CO, USA

13 *Deceased as of 27 May 2014

14
15
16
17
18
19
20
21 Under review in *Atmospheric Chemistry and Physics*

23 **Abstract**

24 Top-down estimates of the spatiotemporal variations in emissions and uptake of CO₂ will benefit
25 from the increasing measurement density brought by recent and future additions to the suite of in
26 situ and remote CO₂ measurement platforms. In particular, the planned NASA Active Sensing of
27 CO₂ Emissions over Nights, Days, and Seasons (ASCENDS) satellite mission will provide
28 greater coverage in cloudy regions, at high latitudes, and at night than passive satellite systems,
29 as well as high precision and accuracy. In a novel approach to quantifying the ability of satellite
30 column measurements to constrain CO₂ fluxes, we use a portable library of footprints (surface
31 influence functions) generated by the WRF-STILT Lagrangian transport model in a regional
32 Bayesian synthesis inversion. The regional Lagrangian particle dispersion model framework is
33 well suited to make use of ASCENDS observations to constrain fluxes at high resolution, in this
34 case at 1° latitude x 1° longitude and weekly for North America. We consider random
35 measurement errors only, modeled as a function of mission and instrument design specifications
36 along with realistic atmospheric and surface conditions. We find that the ASCENDS
37 observations could potentially reduce flux uncertainties substantially at biome and finer scales.
38 At the grid scale and weekly resolution, the largest uncertainty reductions, on the order of 50%,
39 occur where and when there is good coverage by observations with low measurement errors and
40 the a priori uncertainties are large. Uncertainty reductions are smaller for a 1.57 μm candidate
41 wavelength than for a 2.05 μm wavelength, and are smaller for the higher of the two
42 measurement error levels that we consider (1.0 ppm vs. 0.5 ppm clear-sky error at Railroad
43 Valley, Nevada). Uncertainty reductions at the annual, biome scale range from ~40% to ~75%
44 across our four instrument design cases, and from ~65% to ~85% for the continent as a whole.
45 Tests suggest that the quantitative results are moderately sensitive to assumptions regarding a

46 priori uncertainties and boundary conditions. The a posteriori flux uncertainties we obtain,
47 ranging from 0.01 to 0.06 Pg C yr⁻¹ across the biomes, would meet requirements for improved
48 understanding of long-term carbon sinks suggested by a previous study.

49

50

51 **1. Introduction**

52 Quantification of surface fluxes of CO₂ and other greenhouse gases (GHG) over a range
53 of spatial and temporal scales is of critical importance for understanding the processes that drive
54 source/sink variability and climate-biogeochemistry feedbacks. The need to monitor GHG
55 fluxes also follows from climate policy initiatives such as the Kyoto Protocol and possible
56 follow-on agreements, along with their implementation (e.g., emissions trading and treaty
57 verification). While direct “bottom-up” (inventory) approaches are considered accurate to within
58 10% in the annual mean for fossil fuel CO₂ emissions in North America [*Gurney et al.*, 2009],
59 “top-down” (inverse) methods are the tool of choice to infer CO₂ sources and sinks from the
60 terrestrial biosphere and oceans on a range of scales [*Peters et al.*, 2007]. In the top-down
61 approach, fluxes are inferred from atmospheric CO₂ measurements by means of an atmospheric
62 transport model linking the measurements to fluxes upwind. The availability of abundant and
63 accurate measurements and realistic transport models is key to the success of this approach [e.g.
64 Enting et al., 1995]. Consequently, large investments have been made in establishing reliable
65 measurement networks, including in situ measurements of CO₂ concentrations from the surface,
66 towers, and aircraft (e.g. the NOAA ESRL Carbon Cycle Cooperative Global Air Sampling
67 Network [*Dlugokencky et al.*, 2013], and the Earth Networks Greenhouse Gas Network,
68 <http://ghg.earthnetworks.com/>), and satellite missions dedicated to measurement of CO₂ column
69 amounts. The last include the Greenhouse gases Observing SATellite (GOSAT) launched in
70 2009 [*Yokota et al.*, 2009], the Orbiting Carbon Observatory 2 (OCO-2) launched in 2014 [*Crisp*
71 *et al.*, 2008; *Eldering et al.*, 2012], and the planned Active Sensing of CO₂ Emissions over
72 Nights, Days, and Seasons (ASCENDS) mission recommended by the U.S. National Academy of
73 Sciences Decadal Survey [*NRC*, 2007].

74 The objective of our study is to quantify the ability of ASCENDS column measurements
75 to constrain CO₂ fluxes top-down at relatively high resolution. The ASCENDS active
76 measurement concept offers unique capabilities compared with passive satellite systems that rely
77 on thermal emission or reflected sunlight [Kawa et al., 2010]. These capabilities will enhance
78 spatial and temporal coverage while providing high precision and accuracy. ASCENDS will
79 extend coverage through its ability to sample in small cloud gaps and through thin clouds
80 without interference. In addition, since a lidar-based system does not require the presence of the
81 sun, it allows for observations of high-latitude regions during winter. Measurements can be
82 made both night and day, thereby reducing sampling bias due to (and potentially providing
83 constraints on) diurnal variations in CO₂ fluxes driven by ecosystem respiration and primary
84 production.

85 Global studies of the impact of satellite measurements on top-down estimates of CO₂
86 fluxes, beginning with the study of *Rayner and O'Brien* [2001], have established the benefit of
87 using satellite measurements for constraining CO₂ fluxes at a precision level similar to or better
88 than that provided by existing in situ networks. At present, these approaches estimate the
89 reduction of flux uncertainties stemming from the availability of satellite data using an inverse
90 solution for relatively coarse grid boxes or regions at weekly to monthly resolution [e.g.
91 Houweling et al., 2004; Chevallier et al., 2007; Feng et al., 2009; Baker et al., 2010; Kaminski et
92 al., 2010; Hungershofer et al., 2010; Basu et al., 2013; Deng et al., 2014]. The present study
93 extends these global studies to the regional scale using simulated ASCENDS data. Regional
94 trace gas inversions are well-suited for making use of high-density satellite observations to
95 constrain fluxes at fine scales. Regional transport models are less computationally expensive to
96 run than global transport models for a given resolution, so it is more tractable to run a regional

97 model at high resolution. The more precise determination of source-receptor relationships
98 allows one to solve for fluxes at a finer resolution. This reduces potential “aggregation error”
99 resulting from assuming fixed fine-scale flux patterns when optimizing scaling factors on a
100 coarser scale [Kaminski et al., 2001; Engelen et al., 2002; Gerbig et al., 2003; Bocquet et al.,
101 2011].

102 We use a novel approach for our inversions that facilitates high-resolution evaluation of
103 satellite column measurements. The approach relies on a Lagrangian, or air-mass-following,
104 transport model (as opposed to an Eulerian, or fixed-frame-of-reference, model), run backward
105 in time from the observation points (receptors) using ensembles of particles, to generate
106 footprints describing the sensitivity of satellite CO₂ measurements to surface fluxes in upwind
107 regions. Lagrangian particle dispersion models enable more precise simulation of transport in
108 the near field than gridded transport models, since, in the former, particle locations are not
109 restricted to a grid and meteorological fields are interpolated to the subgrid-scale locations.
110 Thus, filamentation processes, for example, can be resolved [Lin et al., 2003], artificial diffusion
111 over grid cells is avoided, and representation errors [Pillai et al., 2010] are minimized. The
112 Lagrangian approach, implemented in the backward (receptor-oriented) mode, offers a natural
113 way of calculating the adjoint of the atmospheric transport model. The utility of Lagrangian
114 particle dispersion models is well established for regional trace gas flux inversions involving in
115 situ observations [e.g. Gerbig et al., 2003; Lin et al., 2004; Kort et al., 2008, 2010; Zhao et al.,
116 2009; Schuh et al., 2010; Göckede et al., 2010a; Brioude et al., 2011, 2012, 2013; Gourdji et al.,
117 2012; Miller et al., 2012, 2013; McKain et al., 2012; Lauvaux et al., 2012]. A convenient feature
118 of Lagrangian footprints is their portability—they can be shared with other groups and readily
119 applied to different flux models, inversion approaches, and molecular species, thus enabling

120 comparisons based on a common modeling component. In addition, footprints for different
121 measurement platforms can be merged easily in an inversion.

122 In this observing system simulation experiment (OSSE), we utilize the Stochastic Time-
123 Inverted Lagrangian Transport (STILT) particle dispersion model [Lin et al., 2003] driven by
124 meteorological fields from the Weather Research and Forecasting (WRF) model [Skamarock and
125 Klemp, 2008] in a domain encompassing North America, in a Bayesian inversion. The WRF-
126 STILT [Nehrkorn et al., 2010] footprints are used to compute weekly flux uncertainties over a 1°
127 latitude x 1° longitude grid. This study focuses on land-based biospheric fluxes. We report
128 results based on realistic sampling and observation errors for a set of ASCENDS instrument
129 designs and other input data fields for year 2007. Section 2 provides details on our inputs and
130 inversion methods, and presents examples of observation uncertainties, a priori flux
131 uncertainties, and WRF-STILT footprint maps. Section 3 presents posterior flux uncertainty
132 results at various spatial and temporal scales, as well as comparisons with other studies. Section
133 4 discusses target and threshold requirements for instrument design parameters with respect to
134 addressing key scientific questions. It also discusses sensitivity to additional sources of
135 uncertainty and limitations of our analysis, as well as other considerations regarding ASCENDS.
136 Section 5 contains concluding remarks.

137

138

139 **2. Methods**

140 2.1. Inversion Approach

141 We use a Bayesian synthesis inversion method, which optimizes the agreement between
142 model and observed CO₂ concentrations and a priori and a posteriori flux estimates in a least-

143 squares manner [e.g. Enting et al., 1995]. Since we focus on random error levels in constraining
144 the fluxes using ASCENDS observations, we did not perform a full inversion and computed only
145 the a posteriori flux error covariance associated with the inversion solution. The a posteriori flux
146 error covariance matrix is given by

$$147 \hat{\mathbf{S}} = (\mathbf{K}^T \mathbf{S}_\varepsilon^{-1} \mathbf{K} + \mathbf{S}_a^{-1})^{-1}, \quad (1)$$

where

148 \mathbf{K} is the Jacobian matrix describing the sensitivity of concentrations to changes in the state vector
elements (in this case, fluxes)

\mathbf{S}_ε is the observation error covariance matrix

\mathbf{S}_a is the a priori flux error covariance matrix.

149 We directly solve for $\hat{\mathbf{S}}$, the square roots of the diagonal elements of which provide the estimates
150 of the a posteriori flux uncertainties.

151 We solve for flux uncertainties in each land cell on a $1^\circ \times 1^\circ$ grid across North America
152 (from 10°N to 70°N and from 170°W to 50°W). The time span is 5 weeks in each of the 4
153 seasons in 2007 (the first 4 weeks of January, April, July, and October plus the week preceding
154 each of those months). We focus on weekly flux resolution in this study, rather than daily or
155 higher resolution, for computational efficiency. In addition, the Decadal Survey called for a
156 satellite mission that can constrain carbon cycle fluxes at weekly resolution on 1° grids [NRC,
157 2007]. The ASCENDS observations would likely also provide significant constraints on fluxes
158 at higher resolutions such as daily, as suggested by test inversions not reported here.

159 We solve Eq. (1) using the standard matrix inversion function in the Interactive Data
160 Language (IDL) software package. We verified the solution using the alternative singular value
161 decomposition approach [Rayner et al., 1999], again in IDL. Given the large dimensions of the
162 matrices-- more than 15,000 10-s average observations each month and 13,205 weekly flux

163 elements over each 5-week period, the procedure requires large amounts of computer memory
164 but a modest amount of processing time--several hours per monthly inversion on the NASA
165 Center for Climate Simulation high-performance computing system.

166

167 2.2. Observational Sampling and Simulated Measurement Uncertainties

168 We consider candidate lidar wavelengths near 1.57 μm and 2.05 μm [Caron and Durand,
169 2009]. These have peak sensitivities in the mid- and lower troposphere, respectively (Figure 1).

170 Other candidate wavelengths with different vertical sensitivities and error characteristics are
171 possible and could be assessed with the same inversion methodology. We derive the
172 temporal/spatial sampling and random error characteristics for ASCENDS pseudo-data based on
173 real cloud/aerosol and surface backscatter conditions for year 2007 in a method similar to that of
174 Kawa et al. [2010]. Observation locations are taken from Cloud-Aerosol Lidar and Infrared
175 Pathfinder Satellite Observation (CALIPSO) satellite orbit tracks. We use only locations that fall
176 within the domain used in the WRF runs (Section 2.4), excluding those within 400 km of the
177 boundaries to provide adequate WRF coverage to simulate back trajectory calculations inside the
178 domain (Figure 2). The errors are calculated as a function of optical depth (OD) measured by
179 CALIPSO, and surface backscatter calculated from Moderate Resolution Imaging
180 Spectroradiometer (MODIS) satellite reflectance over land or glint backscatter, calculated using
181 10-m analyzed wind speeds [Hu et al., 2008] interpolated to the sample locations, over ocean.
182 Samples with total column cloud plus aerosol OD > 0.7 are rejected. For each wavelength case,
183 the measurement errors at each location are scaled to two possible performance levels: 0.5 ppm
184 and 1.0 ppm error (10 s average) under clear-sky conditions (cloud/aerosol OD = 0) for a
185 reflectivity equal to that at a reference site, Railroad Valley (RRV), Nevada. The errors for each

186 5 km (0.74 s) individual CALIPSO observation point are aggregated over 10 s (67 km) intervals
187 to increase signal-to-noise for the pseudo-data, using the formula $\sigma(10s) = \sqrt{\frac{\sum_{i=1}^N \sigma(5km)_i^2}{N^2}}$,
188 where N is the number of valid 5 km observations across the 10-s span. Such a 10-s,
189 conditionally-sampled measurement is expected to represent the basic ASCENDS CO₂ data
190 granule. The uncertainties in the series of 10-s pseudo-data are assumed to be uncorrelated, i.e.
191 the observation error covariance matrix S_e is diagonal.

192 Examples of the coverage of ASCENDS observations available for analysis and their
193 associated uncertainties (for a reference uncertainty at RRV of 0.5 ppm) are shown in Figure 2
194 over seven-day periods in January and July for the two candidate wavelengths. ASCENDS
195 provides dense coverage over the domain with few large gaps, especially in July. A large
196 majority of the 10 second-average observations have uncertainties of < 2 ppm in all four cases
197 except for 2.05 μ m in January. The uncertainties are especially small over land areas, which is
198 helpful for constraining terrestrial fluxes. The uncertainties are generally larger for 2.05 μ m than
199 for 1.57 μ m (by a factor of 1-1.6 over snow-free land and a factor of 1.6-1.8 over snow-/ice-
200 covered areas) except in ice-free oceanic areas, where the uncertainties are similar (Figure 2e and
201 2f).

202

203 2.3. A Priori Flux Uncertainties

204 We derived a priori flux uncertainties at 1° x 1° resolution from the variability of net
205 ecosystem exchange (NEE) in the Carnegie-Ames-Stanford-Approach (CASA) biogeochemical
206 model coupled to version 3 of the Global Fire Emissions Database (GFED3) [Randerson et al.,
207 1996; van der Werf et al., 2006; 2010]. CASA-GFED is driven with meteorological data from

208 the Modern-Era Retrospective Analysis for Research and Applications (MERRA) [Rienecker et
209 al., 2011]. In the version of CASA used here, a sink of $\sim 100 \text{ Tg C yr}^{-1}$ is induced by crop
210 harvest in the U.S. Midwest that is prescribed based on National Agriculture Statistics Service
211 data on crop area and harvest. We neglected uncertainties in fossil fuel emissions, assuming like
212 most previous inversion studies that those emissions are relatively well known. We ignored
213 oceanic fluxes as well for this study, since their uncertainties are also relatively small [e.g. Baker
214 et al., 2010].

215 The a priori flux uncertainties were specifically derived from the standard deviations of
216 daily mean CASA-GFED NEE over each month in 2007, divided by $\sqrt{7}$ to scale approximately
217 to weekly uncertainties. This approach assumes that the more variable the model fluxes are in a
218 particular grid cell and month, the larger the errors tend to be; the same reasoning has been
219 applied in previous inversion studies to the estimation of model-data mismatch errors [e.g. Wang
220 et al., 2008]. We enlarged the resulting uncertainties uniformly by a factor of 4 to approximate
221 the magnitude of those used in the global ASCENDS OSSE described in Section 3.2 of this
222 paper; these are, in turn, essentially the same as the standard ones of Baker et al. [2010], based
223 on differences between two sets of bottom-up flux estimates. In addition to allowing for better
224 comparison of the two OSSEs, the enlargement by a factor of 4 is consistent with suggestions by
225 biospheric model intercomparisons that the true flux uncertainty is greater than that based on a
226 single model's variability [Huntzinger et al., 2012].

227 Off-diagonal elements of the a priori flux error covariance matrix are filled using spatial
228 and temporal error correlations derived from an isotropic exponential decay model with month-
229 specific correlation lengths (Table 1) estimated from ground-based and aircraft CO_2 data in a
230 North America regional inversion by Gourdji et al. [2012]. Although these correlation lengths

231 are not strictly applicable to our study, which has a different setup from that in the geostatistical
232 inverse modeling system of Gourdji et al., they are nonetheless reasonable estimates in general
233 for the purposes of this study. Note that Gourdji et al. used a 3-hourly flux resolution, so the
234 temporal correlation lengths may be too short for the coarser weekly resolution of our study.
235 Chevallier et al. [2012] show that aggregation of fluxes to coarser scales increases the error
236 correlation length. The analysis by Chevallier et al. [2012] using global flux tower data found a
237 weekly-scale temporal error correlation length of 36 days, longer than the values we use. They
238 found a spatial correlation length of less than 100 km at the site scale (~1 km), increasing to 500
239 km at a 300 km-grid scale; our correlation lengths (100 km-grid) mostly fall within that range.
240 In a test, we used alternative values for the spatiotemporal correlation lengths derived from the
241 Chevallier et al. study, and found that the inversion results are moderately sensitive (Section 4.2).

242 Our CASA-GFED-based a priori flux uncertainties, scaled to approximate the values
243 used by Baker *et al.* [2010], are shown in Figure 3. The largest uncertainties occur generally
244 where the absolute value of NEE is highest, e.g., in the “Corn Belt” of the U.S. in summer. The
245 spatial and seasonal variations exhibit similarities to those of Baker et al.

246

247 2.4. WRF-STILT Model, Footprints, and Jacobians

248 The STILT Lagrangian model, driven by WRF meteorological fields, has features,
249 including a realistic treatment of convective fluxes and mass conservation properties, that are
250 important for accurate top-down estimates of GHG fluxes that rely on small gradients in the
251 measured concentrations [Nehrkorn *et al.*, 2010]. In the present application of STILT
252 (www.stilt-model.org, revision 640), hourly output from WRF version 2.2 is used to provide the
253 transport fields at a horizontal resolution of 40 km with 31 eta levels in the vertical, over a North

254 American domain (Figure 2a). Meteorological fields from the North American Regional
255 Reanalysis (NARR) at 32-km resolution are used to provide initial and boundary conditions for
256 the WRF runs. To prevent drift of the WRF simulations from the analyses, the meteorological
257 fields (horizontal winds, temperature, and water vapor at all levels) are nudged to the NARR
258 analysis every 3 hours with a 1-hour relaxation time and are reinitialized every 24 hours (at 00
259 UTC). Simulations are run out for 30 hours, but only hours 7-30 from each simulation are used
260 to avoid spin-up effects during the first 6 hours. The WRF physics options used here are the
261 same as those described by *Nehrkorn et al.* [2010].

262 A footprint quantitatively describes how much surface fluxes originating in upwind
263 regions contribute to the total mixing ratio at a particular measurement location; it has units of
264 mixing ratio per unit flux. This is to be distinguished from a satellite footprint, the area of earth
265 reflecting the lidar signal. In the current application, footprints are computed for each 5-km
266 simulated observation that passes the cloud/aerosol filter in January, April, July, and October
267 2007 at 3-hour intervals back to 10 days prior to the observation time. Separate footprint maps
268 have been computed for 15 receptor positions above ground level for the purpose of vertically
269 convolving with the lidar weighting functions and producing one weighted-average footprint per
270 measurement. (The receptors are spaced 1 km apart in the vertical from 0.5 to 14.5 km AGL.)
271 This procedure results in ~90,000 footprint calculations per day, placing stringent demands on
272 our computational approach. In this study, STILT simulates the release of an ensemble of 500
273 particles at each receptor in the column.

274 It is important to note that although a footprint is defined for each of the 15 vertical
275 levels, the footprint expresses the sensitivity of the mixing ratio measured at the receptor point
276 located at that vertical level to the surface fluxes upwind, not the fluxes upwind at the same

277 level. So intuitively, the footprints defined for receptor points located at high altitudes (e.g. 12.5,
278 13.5, 14.5 km) are often zero, indicating that a receptor at that upper level is not influenced by
279 surface fluxes inside the domain (within the 10 day span examined here). Conversely, receptor
280 points located at the lowest levels (e.g. 0.5, 1.5, 2.5 km) tend to have large footprints (with
281 values of the order of 10^{-3} ppm/($\mu\text{mol}/\text{m}^2/\text{s}$) or higher), being most influenced by nearby surface
282 fluxes.

283 Figure 4 shows the vertically-weighted footprints of a selected column measurement
284 location (in southern Canada) over 10 days for the 1.57 and 2.05 μm wavelengths. Non-zero
285 footprints occur wherever air observed at the receptor site has been in contact with the surface
286 within the past 10 days. Patterns of vertical and horizontal atmospheric motion explain the
287 somewhat unexpected spatial patterns of the footprints in this particular example, with very high
288 values occurring at a significant distance upwind of the receptor (in the vicinity of Texas and
289 Oklahoma) as well as immediately upwind. Vertical mixing lifts the signature of surface fluxes
290 to higher levels, so that it can be detected by receptors at multiple levels, resulting in a higher
291 value for the vertically-convolved footprint, while slower winds in a particular area, such as
292 Texas and Oklahoma, can result in a larger time-integrated impact of fluxes on the observation.
293 The footprint values are larger for 2.05 μm due to the higher sensitivity of that measurement near
294 the surface, as previously discussed.

295 To construct the Jacobians, \mathbf{K} , that enter Eq. (1), we averaged the footprints of all the 5-
296 km receptor locations within a given 10-s averaging period along the satellite track, including
297 only the land cells. We arranged the averaged footprints in a two-dimensional Jacobian, running
298 across flux time intervals and grid cells in one direction and across observations in the other.
299 (The 3-hour flux intervals associated with each transport run are defined relative to fixed UTC

300 times and not relative to the observation times.) We then aggregated the Jacobian elements to
301 the final flux resolution, e.g., weekly. For any particular month, we solved only for fluxes
302 occurring in the week prior to the beginning of the month and in the first 4 weeks of that month.

303 Figure 5 shows the overall influence of the surface fluxes on the observations during each
304 month (i.e. the average weekly Jacobian values for the $1.57\ \mu\text{m}$ weighting function). Values
305 tend to decrease from west to east, reflecting the general westerly wind direction, which
306 transports CO_2 influences out of the domain more quickly for fluxes occurring closer to the
307 eastern edge than for those farther west. Values also tend to decrease towards the north and
308 northwest and in the southernmost part of the continent: these areas lie close to the edges of the
309 domain shown in Figure 2a. Areas with smaller average footprint values are generally not as
310 well constrained by the observations, as will be discussed later in this paper; thus, our domain
311 boundaries artificially limit flux constraints in certain parts of the continent. Previous regional
312 inversion studies may not have highlighted this issue because they used ground-based
313 observations, whose sensitivities are more confined to near-field fluxes than those of satellite
314 column measurements. We will quantify the impact of the boundaries on average footprint
315 gradients in future work, providing guidance for future studies on optimal sizes and shapes of
316 domains (e.g. shifted eastward) for avoiding large gradients while controlling computational
317 cost.

318 Footprint values are largest in summer, again due to horizontal and vertical motions—
319 winds during this season are relatively light and allow the fluxes to stay inside the domain for a
320 long time, maximizing their integrated influence on observations in the domain, and vertical
321 mixing across the deep boundary layer brings particles over a large portion of the column into
322 contact with the surface.

323 Although WRF-STILT provides the capability to generate and optimize boundary
324 condition influences on observed concentrations, this was not available at the time of this study
325 and, consequently, we neglect uncertainties in the influence of boundary conditions in our
326 standard inversion (discussed further in Section 4.2). Similarly, we neglect uncertainties due to
327 the influence of North American fluxes occurring more than 10 days before a particular
328 observation. Note that fluxes are often transported out of the domain within 10 days, so that
329 these fluxes can only influence the observations via the boundary conditions.

330

331 **3. Results**

332 In the following, we present results for four cases involving different combinations of
333 measurement wavelength and baseline error level: 1.57 μm and 0.5 ppm RRV error (Case 1),
334 1.57 μm and 1.0 ppm (Case 2), 2.05 μm and 0.5 ppm (Case 3), and 2.05 μm and 1.0 ppm (Case
335 4).

336

337 3.1. A Posteriori Flux Uncertainties at the Grid Level

338 A posteriori uncertainties (Figure 6) are smaller than the a priori values (Figure 3), an
339 expected result of the incorporation of observational information. The reduction in uncertainty is
340 often larger in areas that have higher a priori uncertainties, as can be seen more clearly in the
341 maps of percentage reduction in uncertainty in Figure 7. Uncertainty reductions are relatively
342 large year-round in places such as southern Mexico and the Pacific Northwest of the U.S.; in
343 April and October in the southeastern U.S.; and in July in the U.S. Midwest, areas with forest fire
344 emissions in central Canada (appearing as hot spots of uncertainty reduction), and Alaska and
345 western Canada. A priori uncertainties are relatively high in these areas, so that there is more

346 room for observations to tighten the constraint. In contrast, where a priori uncertainties are
347 already small, observations are not able to provide a much tighter constraint.

348 Of course, the uncertainty reductions are not dependent simply on the prior uncertainties.
349 For example, the highest uncertainty reductions, up to 50%, occur in southern Mexico in
350 October, where a priori uncertainties are not especially large. The high uncertainty reductions
351 here can be explained by the large Jacobian values (Figure 5) combined with the low
352 uncertainties of nearby observations (not shown). (Although a priori uncertainties and Jacobian
353 values in July in this area are similar to those in October, observation uncertainties are higher,
354 resulting in lower uncertainty reductions.) The tendency of uncertainty reductions to be higher
355 where average Jacobian values are larger can also be seen in the similarity of the spatial patterns
356 in the January maps in Figures 5a and 7a, for example. As described in Section 2.4, fluxes in
357 western and central areas of the continent are captured by more observations in the domain than
358 fluxes in the east and close to the other edges; thus, the former can be better constrained in this
359 inversion.

360 In July, the largest uncertainty reductions occur in northern Alaska and northwestern
361 Canada, which have much smaller a priori uncertainties than places such as the Midwest. This is
362 an effect of the smaller grid cells at higher latitudes: the a priori errors are correlated over larger
363 numbers of cells at these latitudes given the spatially uniform correlation lengths we specify, so
364 that the average flux over each cell is more tightly constrained than that for an otherwise
365 comparable cell at lower latitudes. This is a less important issue when results are aggregated to
366 the larger scales dealt with in later sections of this paper.

367 Uncertainty reductions are smallest in January, for several reasons: 1) a priori flux
368 uncertainties are smallest during the dormant season, 2) observation errors are largest in winter

369 due to the low reflectance of snow and ice cover at the measurement wavelengths, and 3) there is
370 fast dispersion of fluxes in winter by strong winds, transporting fluxes out of the domain and out
371 of detection by observations in the domain and thus reducing the average Jacobian values in
372 January relative to the other months (Figure 5). The ratio of the average of the Jacobian
373 elements over the domain for January to that for July is 0.51 for the 1.57 μm wavelength.

374 Inversions for the 2.05 μm wavelength, with its higher sensitivity near the surface, result
375 in greater uncertainty reduction, despite the larger observation errors over land (Figure 8c vs. 8a,
376 and 8d vs. 8b). Inversions assuming 1.0 ppm instead of 0.5 ppm error at RRV result in less
377 uncertainty reduction (Figure 8b vs. 8a, and 8d vs. 8c) as expected, with maximum uncertainty
378 reduction of $\sim 30\%$ vs. $\sim 40\%$, for 1.57 μm . These cases are compared further in the section
379 below on biome-aggregated results.

380

381 3.2. Results Aggregated to Biomes and Continent, and Compared with Other Inversion Systems

382 For assessing large-scale changes in carbon sources and sinks, it is useful to aggregate
383 high-resolution results to biomes and the entire continent, and to seasons and years. We use the
384 biome definitions in Figure 9 taken from Olson et al. [2001] with modifications by Gourdji et al.
385 [2012]. To aggregate the flux uncertainties, we summed up the variances within each biome and
386 over each month and then the year (in units of $(\text{Pg C yr}^{-1})^2$) as well as the error covariances
387 between grid cells and weeks.

388 We compare our results with those from two other inversion systems: a global inversion
389 using ASCENDS observations (companion study to this one), and a North America regional
390 inversion using the same WRF-STILT Lagrangian model as ours but with a network of ground-
391 based observation sites [Gourdji et al., 2012]. The global OSSE uses the same ASCENDS

392 dataset sampling and underlying observation error model as the regional OSSE. Among the
393 primary differences are the global domain of the analysis (and thus the use of observations
394 outside of the N. American domain as well as inside) and the coarser spatial resolution of the
395 transport and flux solution, 4.5° latitude x 6° longitude. Other differences include the
396 mathematical technique of the inversion (variational data assimilation, as in an earlier study
397 [Baker et al., 2010]), the Eulerian transport model (PCTM; Kawa et al. [2004]), the spatial
398 patterns of the a priori flux uncertainties (the overall magnitudes are not different, as described in
399 Section 2.3), the assumption of zero a priori error correlations, and the use of (estimate - truth)
400 statistics as a proxy for flux uncertainty [Baker et al., 2010], given that the variational method
401 does not directly compute a full a posteriori error covariance matrix. We aggregated the global
402 inversion results to the same biomes, summing the (estimate - truth) values and accounting for
403 fractional biome coverage in each of the coarse grid cells. Gourdji et al. used a set of ground-
404 based and aircraft measurements and a geostatistical inverse model to solve for biospheric fluxes
405 and their uncertainties at a $1^\circ \times 1^\circ$, 3-hourly resolution in 2004. We present these comparisons
406 mainly to provide context for our results, rather than to quantitatively analyze effects of various
407 methodological differences.

408 Uncertainty reductions are largest in July and smallest in January, at the continental scale
409 (Table 2). The uncertainty reductions for the $1.57 \mu\text{m}$ wavelength are on average 8% smaller
410 than those for $2.05 \mu\text{m}$. The uncertainty reductions for the $1.57 \mu\text{m}$ wavelength with 0.5 ppm
411 error are larger than those for $2.05 \mu\text{m}$ with 1.0 ppm error. The uncertainty reductions for 0.5
412 ppm error are on average 16% larger than those for 1.0 ppm error.

413 At the annual, biome scale, our uncertainty reductions range from 50% for the desert
414 biome (averaged across the cases) to 70% for the temperate grassland/shrubland biome (Figure

415 10c). The reductions scale with increasing a priori uncertainty (Figure 10a) and observation
416 quality and density, as before, and now also with biome area (Figure 10d). We find a modest
417 correlation between uncertainty reduction and area in the set of biomes here, with a linear
418 correlation coefficient of 0.5. In addition, the uncertainty reduction is higher on the continental
419 scale than on the biome scale. The a posteriori uncertainty increases with increasing area more
420 slowly than does the a priori uncertainty since many of the a posteriori error covariance terms
421 that are summed in the aggregation to biome are negative, whereas all of the a priori error
422 covariance terms are positive or zero. This explains why uncertainty reduction tends to increase
423 with increasing area.

424 Our a posteriori uncertainties range from 0.12 to 0.33 Pg C yr⁻¹ at the monthly,
425 continental scale across all four cases (Table 2), from 0.04 to 0.08 Pg C yr⁻¹ at the annual,
426 continental scale (Figure 10a), and from 0.01 to 0.06 Pg C yr⁻¹ at the annual, biome scale (Figure
427 10a). To put these numbers into perspective, the estimated current global terrestrial sink is
428 roughly 2.5 Pg C yr⁻¹ [Le Quéré et al., 2012]. Our uncertainties are generally similar to those
429 from the North American regional inversion of Gourdji et al. [2012] (Figure 10a) and the global
430 inversion (Figure 10b), a notable exception being the overall continental result of Gourdji et al.
431 Our a posteriori uncertainty for N. America is small compared to Gourdji et al., likely because of
432 the greater spatial coverage of ASCENDS as compared to the in situ network; some of the
433 biomes are not well constrained by the in situ network (i.e. the ones for which Gourdji et al. did
434 not report aggregated results). Note that the comparison is not totally consistent, given the
435 methodological differences. The global inversion's method for estimating uncertainties based on
436 (estimate - truth) statistics cannot provide an annual uncertainty estimate for the one-year
437 inversion and produces somewhat noisy results for individual months. Therefore, to compare the

438 regional and global inversions, we took the RMS of the four monthly uncertainties. The
439 uncertainty reduction for our regional inversion is similar on average to that of the global
440 inversion across biomes and also for the continent as a whole for Case 1 (Figure 10c), with
441 continent-level values of 78% and 72%, respectively. There are larger differences between the
442 regional and global inversions for particular biomes. Although differences in prior uncertainty
443 (Figure 10b) could possibly explain the differences in uncertainty reduction for some of the
444 biomes (subtropical/tropical, eastern temperate, temperate coniferous, desert), they do not for the
445 others (boreal, tundra, temperate grassland/shrubland), suggesting that prior uncertainties are not
446 the only factor producing the spatial pattern in the comparison.

447

448

449 **4. Discussion**

450 4.1. Target and Threshold Requirements

451 We now discuss the implications of our analysis for the ASCENDS design.
452 Hungershofer et al. [2010] suggested levels of posterior flux uncertainty on different
453 spatiotemporal scales that global CO₂ measurement missions should strive for to allow for
454 answering key carbon cycle science questions. In the following, we evaluate our results relative
455 to those requirements, the only such specific guidelines for CO₂ satellite missions in the
456 scientific literature.

457 Hungershofer et al. suggested that to determine where the global terrestrial C sink is
458 occurring and whether C cycle feedbacks are occurring requires annual net carbon flux estimates
459 with a precision better than 0.1 Pg C yr⁻¹ (threshold) or 0.02 Pg C yr⁻¹ (target) at a scale of 2000
460 x 2000 km, similar to the biomes we consider. These precision levels are based on the range of

461 estimated fluxes across various biomes. The proposed A-SCOPE active CO₂ measurement
462 mission defined a similar target requirement—0.02 Pg C yr⁻¹ at a scale of 1000 x 1000 km
463 [Ingmann et al., 2008]. According to our results (Figure 10a), all tested ASCENDS cases would
464 meet the minimum threshold requirement across all biomes easily, with a posteriori uncertainties
465 ranging from 0.01 to 0.06 Pg C yr⁻¹. In addition, the two cases with 0.5 ppm error would meet
466 the more stringent target requirement for a majority of biomes, while the two cases with 1.0 ppm
467 error would meet it for 3 out of 7 biomes. The meeting of the target requirement is a
468 consequence of the information provided by the observations and not merely an effect of the
469 specified a priori uncertainty, given that the a priori uncertainty is higher than the target level for
470 all of the biomes with the exception of desert, the prior uncertainty for which is already at the
471 target level. One measure of the contribution of the observations to meeting the target is shown
472 in Figure 10e, which is a plot of the fractional uncertainty reduction necessary for different
473 biomes to meet the target. The amounts are mostly greater than 50%, ranging up to 85% for
474 eastern temperate.

475

476 4.2. Sensitivity Tests: Boundary Conditions, A Priori Uncertainties, and Correlation Lengths

477 A simplifying assumption in our standard inversion is the neglect of uncertainties in the
478 boundary conditions (b.c.). It is especially important in a regional inversion (Eulerian or
479 Lagrangian) to accurately account for the influence of lateral boundary inflow on concentrations
480 within the domain [Göckede et al., 2010b; Lauvaux et al., 2012; Gourdji et al., 2012]. Because
481 we neglect b.c. uncertainties, we essentially assume that all of the information in the ASCENDS
482 observations can be applied to reducing regional flux uncertainties rather than the combination of

483 b.c. and flux uncertainties. Thus, the amount of flux uncertainty reduction reported for our
484 standard inversion may be higher than it would be if we accounted for b.c. uncertainties.

485 We conducted a test inversion for July (1.57 μm and 0.5 ppm error case) in which b.c. are
486 added as parameters (specifically, weekly average CO_2 mixing ratios over each of the four lateral
487 walls of the domain) to be estimated in the state, with corresponding elements added to the
488 Jacobian. Given that the actual Jacobian values are not available, we prescribed values that are
489 somewhat realistic: 0.5 ppm ppm^{-1} if an observation occurs in the same week as or after a b.c.,
490 and 0 if an observation occurs before a b.c. We assumed a priori uncertainties of 1 ppm for the
491 b.c., with no correlations among b.c. uncertainties or between b.c. and flux uncertainties. As
492 expected, the reductions in flux uncertainty are smaller than the ones reported above, although
493 the differences are only a factor of 0.01 or less. Weekly uncertainties for the b.c. are reduced by
494 7-13%. A different experimental setup (e.g. larger Jacobian values for the b.c. or a larger
495 number of disaggregated b.c. parameters) could potentially result in a much larger effect on the
496 flux uncertainty reductions.

497 In addition to containing random errors, b.c. can also be a source of systematic errors.
498 For example, Gourdji et al. [2012] found that two plausible sets of b.c. around North America
499 generated inferred fluxes that differed by 0.7-0.9 Pg C/yr on the annual, continental scale (which
500 is a very large amount compared to the annual a posteriori uncertainties for North America of
501 0.04-0.08 Pg C yr^{-1} that we estimated in our OSSE (Figure 10a)). They concluded that b.c. errors
502 may be the primary control on flux errors in regional inversions at this coarse scale, while other
503 factors such as flux resolution, priors, and model transport are more important at sub-domain
504 scales.

505 Sparseness of observations has been a major cause of uncertainty in the boundary
506 influence in previous regional inversions. Lauvaux et al. [2012], who conducted mesoscale
507 inversions for the U.S. Midwest using tower measurements, found b.c. errors to be a significant
508 source of uncertainty in the C budget over 7 months. They estimated that a potential bias of 0.55
509 ppm in their b.c. translates into a flux error of 24 Tg C over 7 months in their 1000 km x 1000
510 km domain. Although they applied corrections to the model-derived b.c. using weekly aircraft
511 profiles at four locations near their domain boundaries, they stated that the b.c. uncertainties
512 were still large given the limited duration (a few hours per week) and spatial extent of the
513 airborne observations, and concluded that additional observations would be necessary to reduce
514 the uncertainties. ASCENDS is promising in this respect, as it (along with other satellites) will
515 provide more frequent and widespread observations of concentrations at regional boundaries,
516 possibly lessening the role of b.c. in the overall C budget uncertainty to a minor one. ASCENDS
517 observations could specifically be used in a global CO₂ data assimilation system to provide
518 accurate b.c. for the regional flux inversion.

519 Posterior uncertainties are generally sensitive to the assumed prior uncertainties, although
520 one might expect the sensitivity to not be so great in the case of a dense observational data set
521 such as the one examined here. We test this hypothesis with an alternative prior uncertainty
522 estimate, one that is uniformly larger than that for the standard inversion by a factor of 2. Figure
523 11a-d shows the ratio of the posterior uncertainty for the large-priors inversion to that for the
524 standard inversion, normalized by a factor of 2. Large areas of the domain have ratios
525 significantly less than 1, especially in July and October. Where the ratio is close to 1, the
526 posterior uncertainty is sensitive to the prior, indicating that the observations have a relatively
527 weak influence; where the ratio is significantly less than 1, the posterior uncertainty is not so

528 sensitive to the prior. The test demonstrates that the posterior uncertainty in many areas is not
529 highly sensitive to the prior uncertainty and is strongly influenced by the observations.
530 However, the sensitivity is high in the tundra and the desert, due to the tight (small) prior
531 constraints in those regions (Figure 3).

532 Although the posterior uncertainty is not highly sensitive to the prior in all areas, it still
533 increases everywhere in the large-priors inversion relative to the standard inversion, implying
534 that our findings regarding whether or not the observations meet the target requirement (Section
535 4.1) are dependent on the assumed priors. However, our standard priors are already enlarged
536 uniformly by a factor of 4 relative to one set of prior uncertainty estimates, and they would have
537 to be enlarged further over large areas to substantially increase biome-level posterior
538 uncertainties. In addition, the larger the prior uncertainties are, the larger the uncertainty
539 reductions are in general. Wherever the posterior uncertainty increases by a smaller factor than
540 does the prior uncertainty (e.g. where the ratio is less than 1 in Figure 11), the uncertainty
541 reduction increases. Altogether, the results of this sensitivity test suggest that it is important to
542 consider different measures of the impact of observations on flux estimates, such as posterior
543 uncertainty and uncertainty reduction, as we have done in this OSSE, given that different
544 measures can be affected differently by assumptions such as prior uncertainties.

545 The inversion results are potentially sensitive to the assumed a priori flux error
546 correlation lengths, with longer correlation lengths leading to more smooth uncertainty reduction
547 patterns and larger uncertainty reductions. Rodgers [2000] shows that the inclusion of a priori
548 error correlations can result in more “degrees of freedom for signal,” i.e. more information
549 provided by the measurements on the unknowns. We carried out a test with alternative values
550 for the correlation lengths derived from the study by Chevallier et al. [2012]—a shorter spatial

551 correlation length of 200 km and a longer temporal correlation length of 35 days, for all months.
552 (We estimated these values from Figure 5a and b of Chevallier et al. for the ~100 km and 7-day
553 aggregation of our inversion.) The resulting uncertainty reductions are smaller everywhere than
554 those in our standard inversion at the grid scale, with values of up to 40% in July and up to 15%
555 in January for Case 1 (compared to 45% and 25%, respectively, in the standard inversion).
556 Apparently, the decrease in the spatial correlation length relative to the standard inversion has a
557 larger effect than the increase in the temporal correlation length. Aggregated to the continent
558 and month, the uncertainty reduction is less than that for the standard inversion for all months
559 except July, for which the uncertainty reduction is marginally larger (Table 2). For July, the
560 impact of the much longer temporal correlation length relative to the standard inversion on the
561 aggregated result more than offsets that of the slightly shorter spatial correlation length. The
562 annual uncertainty reduction for the alternative inversion is slightly larger than that for the
563 standard inversion, because of the disproportionate influence of July, with its large a priori
564 uncertainty. We conclude that our inversion results vary moderately given two reasonable sets
565 of estimates for the a priori spatiotemporal error correlation lengths.

566

567 4.3. Other Sources of Error

568 This analysis did not evaluate the impact of potential systematic errors (biases) in the
569 observations or the transport model, which are not well represented by the Gaussian errors
570 assumed in traditional linear error analysis [Baker et al., 2010]. Chevallier et al. [2007]
571 demonstrated that potential biases in OCO satellite CO₂ measurements related to the presence of
572 aerosols can completely negate the improvements to prior uncertainties provided by the
573 measurements for the most polluted land regions and for ocean regions. In another OCO OSSE,

574 Baker et al. [2010] found that a combination of systematic errors from aerosols, model transport,
575 and incorrectly-assumed statistics could degrade both the magnitude and spatial extent of
576 uncertainty improvements by about a factor of two over land, and even more over the ocean.
577 Thus, it will be important to control systematic errors in ASCENDS observations and the
578 transport model as well as minimizing random errors. Note that systematic observation errors
579 can be expected to decrease over the course of the mission as adjustments are made to the
580 measurement system and to the retrieval algorithms in calibration/validation activities.

581

582 4.4. Other Considerations in Evaluating ASCENDS

583 The potential combined use of multiple wavelengths in the ASCENDS measurements,
584 e.g., various offsets from 1.57 μm , could provide additional information on surface fluxes given
585 the sensitivities to concentrations at different levels of the atmosphere. Furthermore, other CO_2
586 datasets will certainly be available alongside the ASCENDS data (e.g. from in situ networks),
587 and the combination of datasets will provide stronger constraints on fluxes than any individual
588 dataset [Hungershoefer et al., 2010].

589 Our comparison of the results for the 1.57 and 2.05 μm wavelengths over North America
590 may be less applicable to other parts of the world. The global OSSE study by Hungershoefer et
591 al. [2010], which compared various observing systems, including a satellite lidar system similar
592 to ASCENDS, A-SCOPE, found that the 1.6 μm wavelength results in larger uncertainty
593 reductions over South America while performing less well than 2.0 μm over temperate and cold
594 regions. They attribute the better performance of 1.6 μm over South America to the strong
595 vertical mixing of air there, which lessens the disadvantage of that wavelength's having weaker
596 sensitivity to the lower troposphere. (However, they used a simpler error formulation.) On the

597 other hand, in our global inversion, 2.05 μm results in larger uncertainty reductions than 1.57 μm
598 throughout the world, by 8% on average (for RRV error of 0.5-1.0 ppm).

599

600

601 **5. Conclusions**

602 We have conducted an observing system simulation for North America, using projected
603 ASCENDS observation uncertainty estimates and a novel approach utilizing a portable footprint
604 library generated from a high-resolution Lagrangian transport model, to quantify the surface CO_2
605 flux constraints provided by the future observations. We consider four possible configurations
606 for the active optical remote sensing instrument covering two weighting functions and two
607 random error levels. We find that the ASCENDS observations potentially reduce flux
608 uncertainties substantially at fine and biome scales. At the $1^\circ \times 1^\circ$ grid scale, weekly uncertainty
609 reductions up to 30-45% (averaged over the year) are achieved depending on the presumed
610 instrument configuration. Relatively large uncertainty reductions occur year-round in southern
611 Mexico and the Pacific Northwest and seasonally in the southeastern and mid-western U.S. and
612 parts of Canada and Alaska, when and where there is good coverage by observations with low
613 uncertainties and a priori uncertainties are large. Uncertainty reductions at the annual, biome
614 scale range from ~40% to ~75% across the four experimental cases, and from ~65% to ~85% for
615 the continent as a whole. The uncertainty reductions for the 1.57 μm candidate wavelength are
616 on average 10% smaller than those for 2.05 μm across the biomes and the two RRV reference
617 error levels, and for 0.5 ppm RRV error are on average ~25% larger than those for 1.0 ppm error
618 across biomes and the two wavelengths.

619 Based on the flux precision on an annual, biome scale suggested by Hungershoefer et al.
620 [2010] for understanding the global carbon sink and feedbacks, ASCENDS observations would
621 meet a threshold requirement for all biomes within the range of measurement designs considered
622 here. The observations constrain a posteriori uncertainties to a level of 0.01-0.06 Pg C yr⁻¹, and
623 could thus help pin down the location and magnitude of long-term C sinks. With regards to the
624 more stringent target requirement, a subset of the instrument designs would meet the target for a
625 majority of biomes.

626 The results we have presented may be optimistic, as potential systematic errors in the
627 observations, boundary conditions, and transport model that we have neglected would degrade
628 the flux estimates. Modifications to the size and location of our regional domain, however, e.g.
629 an eastward shift, could improve the constraints by satellite observations on North American
630 fluxes. In addition, our consideration of different measures of the impact of observations on flux
631 estimates, such as posterior uncertainty and uncertainty reduction, strengthens the study, given
632 that different measures can be affected differently by assumptions such as prior uncertainties.

633 In future work, inversions in various regions (including, for example, South America)
634 with a more comprehensive treatment of error sources could more definitively establish the
635 usefulness of ASCENDS observations for constraining fluxes at fine and large scales and
636 answering global carbon cycle science questions.

637

638

639 **Acknowledgments**

640 Work at NASA and AER has been supported by the NASA Atmospheric CO₂ Observations from
641 Space program element and NASA ASCENDS Pre-Phase A activity funding. We are grateful to

642 the NASA Ames HEC facility staff for assistance in executing the WRF-STILT runs on the
643 Pleiades supercomputer, and to the NASA HEC Program for granting use of the Dali and
644 Discover systems at the NASA Center for Climate Simulation. We also thank J. Abshire, E.
645 Browell, and R. Menzies for contributions to ASCENDS data characterization, G. J. Collatz for
646 making available the CASA-GFED fluxes that we used to construct the a priori uncertainties, R.
647 Aschbrenner for help with the footprint calculations, S. Gourджи for providing correlation
648 parameters and the biome map, P. Rayner and A. Michalak for advice on inversions, M. Manyin
649 and Y. Liu for computing help, L. Ott for help with transferring WRF-STILT files, and G. J.
650 Collatz and E. McGrath-Spangler for comments on the manuscript. Finally, we appreciate the
651 comments provided by two anonymous referees.

652

653 **References**

654

655 Baker, D. F., Boesch, H., Doney, S. C., O'Brien, D., and Schimel, D. S. (2010), Carbon
656 source/sink information provided by column CO₂ measurements from the Orbiting Carbon
657 Observatory, *Atmos. Chem. Phys.*, *10*, 4145–4165, doi:10.5194/acp-10-4145-2010.

658 Basu, S., S. Guerlet, A. Butz, S. Houweling, O. Hasekamp, I. Aben, P. Krummel, P. Steele, R.
659 Langenfelds, M. Torn, S. Biraud, B. Stephens, A. Andrews, and D. Worthy (2013), Global
660 CO₂ fluxes estimated from GOSAT retrievals of total column CO₂, *Atmos. Chem. Phys.*, *13*,
661 8695–8717, doi:10.5194/acp-13-8695-2013.

662 Bocquet, M., Wu, L., Chevallier, F. 2011. Bayesian design of control space for optimal
663 assimilation of observations. Part I: Consistent multiscale formalism. *Q. J. R. Meteorol. Soc.*
664 **137**: 1340–1356. doi:10.1002/qj.837.

665 Brioude, J., Kim, S.-W., Angevine, W. M., Frost, G. J., Lee, S-H, McKeen, S. A., Trainer, M.,
666 Fehsenfeld, F. C., Holloway, J. S., Ryerson, T. B., Williams, E. J., Petron, G., and Fast, J. D.
667 (2011), Top-down estimate of anthropogenic emission inventories and interannual variability
668 in Houston using a mesoscale inverse modeling technique, *J. Geophys. Res.*, *116*, D20305,
669 doi:10.1029/2011JD016215.

670 Brioude, J., Petron, G., Frost, G. J., Ahmadov, R., Angevine, W. M., Hsie, E. -Y., Kim, S. -W.,
671 Lee, S. -H., McKeen, S. A., Trainer, M., Fehsenfeld, F. C., Holloway, J. S., Peischl, J.,
672 Ryerson, T. B., and Gurney, K. R. (2012), A new inversion method to calculate emission
673 inventories without a prior at mesoscale: Application to the anthropogenic CO₂ emission
674 from Houston, Texas, *J. Geophys. Res.*, *117*, D05312, doi:10.1029/2011JD016918.

675 Brioude, J., Angevine, W. M., Ahmadov, R., Kim, S. -W., Evan, S., McKeen, S. A., Hsie, E. -Y.,
676 Frost, G. J., Neuman, J. A., Pollack, I. B., Peischl, J., Ryerson, T. B., Holloway, J., Brown, S.
677 S., Nowak, J. B., Roberts, J. M., Wofsy, S. C., Santoni, G. W., Oda, T., and Trainer, M.
678 (2013), Top-down estimate of surface flux in the Los Angeles Basin using a mesoscale
679 inverse modeling technique: assessing anthropogenic emissions of CO, NO_x and CO₂ and
680 their impacts, *Atmos. Chem. Phys.*, 13, 3661-3677, doi:10.5194/acp-13-3661-2013.

681 Butler, M. P., Davis, K. J., Denning, A. S., and Kawa, S. R. (2010), Using continental
682 observations in global atmospheric inversions of CO₂: North American carbon sources and
683 sinks, *Tellus*, 62B, 550–572, doi:10.1111/j.1600-0889.2010.00501.x.

684 Caron, J. and Y. Durand (2009), Operating wavelengths optimization for a spaceborne lidar
685 measuring atmospheric CO₂, *Appl. Opt.* 48, 5413-5422.

686 Chevallier, F., F.-M. Bréon, and P. J. Rayner (2007), Contribution of the Orbiting Carbon
687 Observatory to the estimation of CO₂ sources and sinks: Theoretical study in a variational
688 data assimilation framework, *J. Geophys. Res.*, 112, D09307, doi:10.1029/2006JD007375.

689 Crisp, D., Miller, C. E., and DeCola, P. L. (2008), NASA Orbiting Carbon Observatory:
690 measuring the column averaged carbon dioxide mole fraction from space, *J. Appl. Remote*
691 *Sens.*, 2, 023508, doi:10.1117/1.2898457.

692 Deng, F., D. B. A. Jones, D. K. Henze, N. Bousserrez, K. W. Bowman, J. B. Fisher, R. Nassar, C.
693 O'Dell, D. Wunch, P. O. Wennberg, E. A. Kort, S. C. Wofsy, T. Blumenstock, N. M.
694 Deutscher, D. W. T. Griffith, F. Hase, P. Heikkinen, V. Sherlock, K. Strong, R. Sussmann,
695 and T. Warneke (2014), Inferring regional sources and sinks of atmospheric CO₂ from
696 GOSAT XCO₂ data, *Atmos. Chem. Phys.*, 14, 3703–3727, doi:10.5194/acp-14-3703-2014.

697 Dlugokencky, E.J., P.M. Lang, K.A. Masarie, A.M. Crotwell, and M.J. Crotwell (2013),
698 Atmospheric Carbon Dioxide Dry Air Mole Fractions from the NOAA ESRL Carbon Cycle
699 Cooperative Global Air Sampling Network, 1968-2012, Version: 2013-08-28, Path:
700 ftp://aftp.cmdl.noaa.gov/data/trace_gases/co2/flask/surface/.

701 Elderling, A., Solish, B., Kahn, P., Boland, S., Crisp, D., and Gunson, M. (2012), High Precision
702 Atmospheric CO₂ Measurements from Space: The Design and Implementation of OCO-2,
703 IEEE Aerospace Conference Proceedings, 1805-1814.

704 Engelen, R. J., Denning, A. S., and Gurney, K. R.: On error estimation in atmospheric CO₂
705 inversions, *J. Geophys. Res.*, 107, 4635, doi:10.1029/2002JD002195, 2002.

706 Enting, I. G., Trudinger, C. M. and Francey, R. J. (1995), A synthesis inversion of the
707 concentration and $\delta^{13}\text{C}$ of atmospheric CO₂. *Tellus 47B*, 35–52.

708 Feng, L., Palmer, P. I., Boesch, H., and Dance, S.: Estimating surface CO₂ fluxes from space-
709 borne CO₂ dry air mole fraction observations using an ensemble Kalman Filter, *Atmos.*
710 *Chem. Phys.*, 9, 2619–2633, doi:10.5194/acp-9-2619-2009, 2009.

711 Gerbig, C., J. C. Lin, S. C. Wofsy, B. C. Daube, A. E. Andrews, B. B. Stephens, P. S. Bakwin,
712 and C. A. Grainger (2003), Towards constraining regional scale fluxes of CO₂ with
713 atmospheric observations over a continent: 2. Analysis of COBRA data using a receptor-
714 oriented framework, *J. Geophys. Res.*, 108 (D24), 4757, doi:10.1029/2003JD003770.

715 Göckede, M., Michalak, A. M., Vickers, D., Turner, D. P., and Law, B. E.: Atmospheric inverse
716 modeling to constrain regional scale CO₂ budgets at high spatial and temporal resolution, *J.*
717 *Geophys. Res.*, 115, D15113, doi:10.1029/2009JD012257, 2010a.

718 Göckede, M., D. P. Turner, A. M. Michalak, D. Vickers, and B. E. Law (2010b), Sensitivity of a
719 subregional scale atmospheric inverse CO₂ modeling framework to boundary conditions, *J.*
720 *Geophys. Res.*, *115*, D24112, doi:10.1029/2010JD014443.

721 Gourdji, S. M., K. L. Mueller, V. Yadav, D. N. Huntzinger, A. E. Andrews, M. Trudeau, G.
722 Petron, T. Nehrkorn, J. Eluszkiewicz, J. Henderson, D. Wen, J. Lin, M. Fischer, C. Sweeney,
723 and A. M. Michalak (2012), North American CO₂ exchange: intercomparison of modeled
724 estimates with results from a fine-scale atmospheric inversion, *Biogeosciences*, *9*, 457–475.

725 Gurney, K.R., D.L. Mendoza, Y. Zhou, M.L. Fischer, C.C. Miller, S. Geethakumar, and S. de la
726 Rue du Can (2009), High Resolution Fossil Fuel Combustion CO₂ Emission Fluxes for the
727 United States, *Environ. Sci. & Technol.* *43* (14), 5535-5541, doi:10.1021/es900806c.

728 Houweling, S., F.-M. Breon, I. Aben, C. Roedenbeck, M. Gloor, M. Heimann, and P. Ciais
729 (2004), Inverse modeling of CO₂ sources and sinks using satellite data: a synthetic inter-
730 comparison of measurement techniques and their performance as a function of space and
731 time, *Atmos. Chem. Phys.*, *4*, 523–538.

732 Hungershofer, K., F.-M. Breon, P. Peylin, F. Chevallier, P. Rayner, A. Klonecki, S. Houweling,
733 and J. Marshall (2010), Evaluation of various observing systems for the global monitoring of
734 CO₂ surface fluxes, *Atmos. Chem. Phys.*, *10*, 10503–10520, doi:10.5194/acp-10-10503-2010.

735 Huntzinger, D. N., Post, W. M., Wei, Y., Michalak, A. M., West, T. O., Jacobson, A. R., Baker,
736 I. T., Chen, J. M., Davis, K. J., Hayes, D. J., Hoffman, F. M., Jain, A. K., Liu, S., McGuire,
737 A. D., Neilson, R. P., Potter, C., Poulter, B., Price, D., Raczka, B. M., Tian, H. Q., Thornton,
738 P., Tomelleri, E., Viovy, N., Xiao, J., Yuan, W., Zeng, N., Zhao, M., and Cook, R.: North
739 American Carbon Program (NACP) Regional Interim Synthesis: Terrestrial Biospheric

740 Model Intercomparison, *Ecol. Model.*, 232, 144–157, doi:10.1016/j.ecolmodel.2012.02.004,
741 2012.

742 Hu, Y., K. Stamnes, M. Vaughan, J. Pelon, C. Weimer, D. Wu, M. Cisewski, W. Sun, P. Yang,
743 B. Lin, A. Omar, D. Flittner, C. Hostetler, C. Trepte, D. Winker, G. Gibson, and M. Santa-
744 Maria, Sea surface wind speed estimation from space-based lidar measurements, *Atmos.*
745 *Chem. Phys.*, 8, 3593-3601, 2008.

746 Ingmann, P.: A-SCOPE, Advanced space carbon and climate observation of planet earth, Report
747 for Assessment, SP-1313/1, ESA communication production office, Noordwijk, The
748 Netherlands, 2008.

749 Kaminski, T., Rayner, P., Heimann, M., and Enting, I.: On aggregation errors in atmospheric
750 transport inversions, *J. Geophys. Res.*, 106(D5), 4703–4715, 2001.

751 Kaminski, T., Scholze, M. and Houweling, S.: Quantifying the benefit of A-SCOPE data for
752 reducing uncertainties in terrestrial carbon fluxes in CCDAS, *Tellus*, 62B(5), 784–796, 2010.

753 Kawa, S. R., D. J. Erickson III, S. Pawson, and Z. Zhu (2004), Global CO₂ transport simulations
754 using meteorological data from the NASA data assimilation system, *J. Geophys. Res.*, 109,
755 D18312, doi:10.1029/2004JD004554.

756 Kawa, S. R., J. Mao, J. B. Abshire, G. J. Collatz, X. Sun, and C. J. Weaver (2010), Simulation
757 studies for a space-based CO₂ lidar mission, *Tellus B*, doi:10.1111/j.1600-
758 0889.2010.00486.x.

759 Kort, E. A. et al. (2008), Emissions of CH₄ and N₂O over the United States and Canada based on
760 a receptor-oriented modeling framework and COBRA-NA atmospheric observations,
761 *Geophys. Res. Lett.*, 35, L18808, doi:10.1029/2008GL034031.

762 Kort E. A. et al. (2010), Atmospheric constraints on 2004 emissions of methane and nitrous
763 oxide in North America from atmospheric measurements and receptor-oriented modeling
764 framework, *J. Integr. Environ. Sci.*, 7:2, 125-133.

765 Lauvaux, T., A. E. Schuh, M. Uliasz, S. Richardson, N. Miles, A. E. Andrews, C. Sweeney, L. I.
766 Diaz, D. Martins, P. B. Shepson, and K. J. Davis: Constraining the CO₂ budget of the corn
767 belt: exploring uncertainties from the assumptions in a mesoscale inverse system, *Atmos.*
768 *Chem. Phys.*, 12, 337–354, doi:10.5194/acp-12-337-2012, 2012.

769 Le Quéré, C., Andres, R. J., Boden, T., Conway, T., Houghton, R. A., House, J. I., Marland, G.,
770 Peters, G. P., van der Werf, G., Ahlström, A., Andrew, R. M., Bopp, L., Canadell, J. G.,
771 Ciais, P., Doney, S. C., Enright, C., Friedlingstein, P., Huntingford, C., Jain, A. K.,
772 Jourdain, C., Kato, E., Keeling, R. F., Klein Goldewijk, K., Levis, S., Levy, P., Lomas, M.,
773 Poulter, B., Raupach, M. R., Schwinger, J., Sitch, S., Stocker, B. D., Viovy, N., Zaehle, S.,
774 and Zeng, N.: The global carbon budget 1959–2011, *Earth Syst. Sci. Data Discuss.*, 5, 1107-
775 1157, doi:10.5194/essdd-5-1107-2012, 2012.

776 Lin, J. C., C. Gerbig, S. C. Wofsy, B. C. Daube, A. E. Andrews, K. J. Davis, and C. A. Grainger
777 (2003), A near-field tool for simulating the upstream influence of atmospheric observations:
778 The Stochastic Time-Inverted Lagrangian Transport (STILT) model, *J. Geophys. Res.*,
779 *108(D16)*, 4493, doi:10.1029/2002JD003161.

780 McKain, K., S. C. Wofsy, T. Nehrkorn, J. Eluszkiewicz, J. R. Ehleringer, and B. B. Stephens
781 (2012), Assessment of ground-based atmospheric observations for verification of greenhouse
782 gas emissions from an urban region, *Proc. Natl. Acad. Sci.*, 109, 8423-8428.

783 Miller, S. M. E. A. Kort, A. I. Hirsch, E. J. Dlugokencky, A. E. Andrews, X. Xu, H. Tian, T.
784 Nehrkorn, J. Eluszkiewicz, A. M. Michalak, and S. C. Wofsy (2012) Regional sources of

785 nitrous oxide over the United States: Seasonal variation and spatial distribution, *J. Geophys.*
786 *Res.*, 117, D06310, doi:10.1029/2011JD016951.

787 Miller, S. M., S. C. Wofsy, A. M. Michalak, E. A. Kort, A. E. Andrews, S. C. Biraud, E. J.
788 Dlugokencky, J. Eluszkiewicz, M. L. Fischer, G. Janssens-Maenhout, B. R. Miller, J. B.
789 Miller, S. A. Montzka, T. Nehrkorn, and C. Sweeney (2013), Anthropogenic emissions of
790 methane in the United States, *Proc. Natl. Acad. Sci.*, 110(50), 20018-20022,
791 doi:10.1073/pnas.1314392110.

792 National Research Council (2007), *Earth Science and Applications from Space: National*
793 *Imperatives for the Next Decade and Beyond*. Washington, DC: The National Academies
794 Press.

795 Nehrkorn, T., J. Eluszkiewicz, S. C. Wofsy, J. C. Lin, C. Gerbig, M. Longo, and S. Freitas
796 (2010), Coupled Weather Research and Forecasting/Stochastic Time-Inverted Lagrangian
797 Transport (WRF-STILT) model, *Meteor. Atmos. Phys.*, 107 (1-2), 51–64,
798 doi:10.1007/s00703-010-0068-x.

799 Olson, D. M., Dinerstein, E., Wikramanayake, E. D., Burgess, N. D., Powell, G. V. N.,
800 Underwood, E. C., D’Amico, J. A., Itoua, I., Strand, H. E., Morrison, J. C., Loucks, C. J.,
801 Allnutt, T. F., Ricketts, T. H., Kura, Y., Lamoreux, J. F., Wettengel, W. W., Hedao, P., and
802 Kassem, K. R.: Terrestrial ecoregions of the world: a new map of life on earth, *Bioscience*,
803 51, 933–938, 2001.

804 Peters, W., A. R. Jacobson, C. Sweeney, A. E. Andrews, T. J. Conway, K. Masarie, J. B. Miller,
805 L. M. P. Bruhwiler, G. Petron, A. I. Hirsch, D. E. J. Worthy, G. R. van der Werf, J. T.
806 Randerson, P. O. Wennberg, M. C. Krol, and P. P. Tans (2007), An atmospheric perspective

807 on North American carbon dioxide exchange: Carbon Tracker, *Proc. Nat. Acad. Sci.*, *104*,
808 18,925-18,930.

809 Pillai, D., Gerbig, C., Marshall, J., Ahmadov, R., Kretschmer, R., Koch, T., and Karstens, U.:
810 High resolution modeling of CO₂ over Europe: implications for representation errors of
811 satellite retrievals, *Atmos. Chem. Phys.*, *10*, 83–94, doi:10.5194/acp-10-83-2010, 2010.

812 Randerson, J. T., M. V. Thompson, and C. M. Malmstrom (1996), Substrate limitations for
813 heterotrophs: Implications for models that estimate the seasonal cycle of atmospheric CO₂,
814 *Global Biogeochem. Cycles*, *10*, 585-602.

815 Rayner, P. J., Enting, I. G., Francey, R. J. and Langenfelds, R. 1999. Reconstructing the recent
816 carbon cycle from atmospheric CO₂, $\delta^{13}\text{C}$ and O₂/N₂ observations. *Tellus* **51B**, 213–232.

817 Rayner, P. J., and D. M. O'Brien (2001), The utility of remotely sensed CO₂ concentration data
818 in surface source inversions, *Geophys. Res. Lett.*, *28*, 175–178.

819 Rienecker, M. M., et al.: MERRA: NASA's Modern-Era Retrospective Analysis for Research
820 and Applications, *J. Climate*, *24*, 3624–3648, 2011.

821 Rodgers, C. D. (2000), *Inverse Methods for Atmospheric Sounding: Theory and Practice*. World
822 Scientific.

823 Schuh, A. E., Denning, A. S., Corbin, K. D., Baker, I. T., Uliasz, M., Parazoo, N., Andrews, A.
824 E., and Worthy, D. E. J. (2010), A regional high-resolution carbon flux inversion of North
825 America for 2004, *Biogeosciences*, *7*, 1625–1644, doi:10.5194/bg-7-1625-2010.

826 Skamarock, W. C. and J. B. Klemp (2008), A time-split nonhydrostatic atmospheric model for
827 weather research and forecasting applications, *J. Comp. Phys.*, *227*, 3465-3485.

828 van der Werf, G. R., J. T. Randerson, L. Giglio, G. J. Collatz, P. S. Kasibhatla, and A. F.
829 Arellano, Jr (2006), Interannual variability in global biomass burning emissions from 1997-
830 2004, *Atmos. Chem. Phys.*, *6*, 3423-3441.

831 van der Werf, G. R., J. T. Randerson, L. Giglio, G. J. Collatz, M. Mu, P. S. Kasibhatla, D. C.
832 Morton, R. S. DeFries, Y. Jin, and T. T. van Leeuwen (2010), Global fire emissions and the
833 contributions of deforestation, savanna, forest, agricultural, and peat fires (1997-2009),
834 *Atmos. Chem. Phys.*, *10*, 11707-11735, doi:10.5194/acp-10-11707-2010.

835 Wang, J. S., M. B. McElroy, J. A. Logan, P. I. Palmer, W. L. Chameides, Y. Wang, and I. A.
836 Megretskaia (2008), A quantitative assessment of uncertainties affecting estimates of global
837 mean OH derived from methyl chloroform observations, *J. Geophys. Res.*, *113*, D12302,
838 doi:10.1029/2007JD008496.

839 Yokota, T., Yoshida, Y., Eguchi, N., Ota, Y., Tanaka, T., Watanabe, H., and Maksyutov, S.
840 (2009), Global Concentrations of CO₂ and CH₄ Retrieved from GOSAT: First Preliminary
841 Results, *SOLA*, *5*, 160–163, doi:10.2151/sola.2009-041.

842 Zhao, C., A. E. Andrews, L. Bianco, J. Eluszkiewicz, A. Hirsch, C. MacDonald, T. Nehrkorn,
843 and M. L. Fischer (2009), Atmospheric inverse estimates of methane emissions from Central
844 California, *J. Geophys. Res.*, *114*, D16302, doi:10.1029/2008JD011671.

845

846 **Table 1.** Spatiotemporal Correlation Parameters Used.

Month	Spatial correlation e-folding length (km)	Temporal correlation e-folding length (days)
January	481	17.2
April	419	7.2
July	284	6.9
October	638	1.6

847

848 **Table 2.** Flux Uncertainties Aggregated to Entire Continent and Month or Year (Pg C yr^{-1}).

	January	April	July	October	Annual
<u>Standard inversion</u>					
A priori	0.42	0.78	1.26	0.82	0.24
A posteriori (uncertainty reduction)					
Case 1	0.24 (43%)	0.17 (78%)	0.15 (88%)	0.2 (76%)	0.05 (78%)
Case 2	0.33 (21%)	0.28 (65%)	0.26 (80%)	0.31 (61%)	0.08 (66%)
Case 3	0.18 (57%)	0.13 (83%)	0.12 (91%)	0.15 (81%)	0.04 (83%)
Case 4	0.28 (35%)	0.22 (72%)	0.2 (84%)	0.25 (69%)	0.07 (73%)
<u>Inversion with alternative correl. lengths (200 km, 35 days)</u>					
A priori	0.23	0.59	1.27	0.59	0.21
A posteriori (uncertainty reduction)					

Case 1 0.17 (25%) 0.15 (74%) 0.14 (89%) 0.16 (73%) 0.04 (80%)

849

850

851 **Figure Captions**

852 **Figure 1.** Vertical weighting functions per ppmv of CO₂ (10^{-6} ppmv⁻¹ hPa⁻¹) for two candidate
853 ASCENDS wavelengths. These relate differential optical depth lidar measurements (on-line
854 minus off-line) to column-average CO₂ mixing ratios. The precise on-line wavelengths used
855 here are 1.571121 μm, which is 10 picometers (pm) offset from line center, and 2.051034 μm.

856 **Figure 2.** Examples of measurement locations (individual 10-s averages) and 10-s uncertainties
857 (1σ) for the 0.5 ppm RRV random error case, across 7 day spans for a) the 1.57 μm wavelength
858 in January and b) in July; and for c) the 2.05 μm wavelength in January and d) in July.

859 Locations with OD > 0.7 are rejected. e) Ratio of uncertainty for 2.05 μm to 1.57 μm in January
860 and f) in July. The WRF domain for the runs utilized in this study is indicated by the bold, black
861 lines in a).

862 **Figure 3.** A priori weekly flux uncertainty for a) January, b) April, c) July, and d) October.

863 Average fractional flux uncertainties over the domain are given in each panel ($F \equiv$ flux). $1 \mu\text{mol}$
864 $\text{m}^{-2} \text{s}^{-1} = 1.037 \text{ g C m}^{-2} \text{ d}^{-1} = 4.4 \times 10^{-8} \text{ kg CO}_2 \text{ m}^{-2} \text{ s}^{-1}$.

865 **Figure 4.** Footprint maps for one simulated ASCENDS measurement location (marked by black
866 star) on January 1, 2007 at 18 UTC, integrated over 10 days and convolved over the 500-14500
867 m AGL range with two candidate ASCENDS weighting functions: for the CO₂ laser lines at 2.05
868 μm (top) and 1.57 μm (bottom). Units are ppm/(μmol/m²/s). Note that the native temporal
869 resolution of the footprints is 3 hours; the 10-day integral in this figure is for illustrative purposes
870 only. Only footprints over land are used in the analysis.

871 **Figure 5.** Jacobian values averaged over all observations and weekly flux intervals for a)
872 January, b) April, c) July, and d) October, for the 1.57 μm weighting function.

873 **Figure 6.** A posteriori weekly flux uncertainty over a) January, b) April, c) July, and d) October,
874 for Case 1 (1.57 μm and 0.5 ppm RRV error). Shown here are RMS values from the first 4
875 weeks of each month. $1 \mu\text{mol m}^{-2} \text{ s}^{-1} = 1.037 \text{ g C m}^{-2} \text{ d}^{-1} = 4.4 \times 10^{-8} \text{ kg CO}_2 \text{ m}^{-2} \text{ s}^{-1}$.

876 **Figure 7.** Weekly fractional flux uncertainty reduction over a) January, b) April, c) July, and d)
877 October, for Case 1 (1.57 μm and 0.5 ppm RRV error). Shown here are results from the first 4
878 weeks of each month.

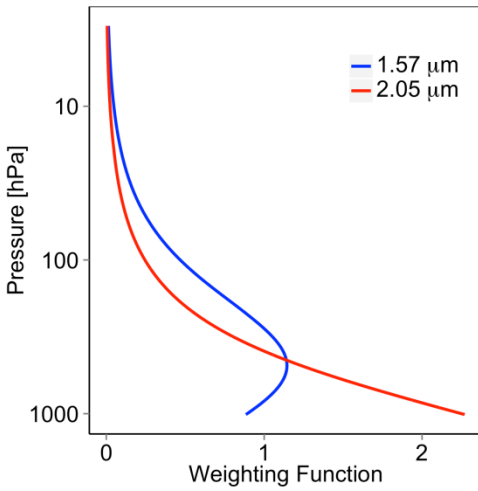
879 **Figure 8.** Weekly fractional flux uncertainty reduction (RMS over the 4 months) for a) Case 1
880 (1.57 μm and 0.5 ppm RRV error), b) Case 2 (1.57 μm and 1.0 ppm), c) Case 3 (2.05 μm and 0.5
881 ppm), and d) Case 4 (2.05 μm and 1.0 ppm).

882 **Figure 9.** Biomes used, taken from Olson et al. [2001] with modifications by Gourджи et al.
883 [2012].

884 **Figure 10.** Results aggregated to biomes and continent, and compared with other studies. a) A
885 priori and a posteriori uncertainties for the year, including results from Gourджи et al. [2012]. b)
886 RMS of the four monthly uncertainties, including results from the global inversion. c) Fractional
887 uncertainty reductions. d) Land area of the biomes. Gourджи et al. reported results for only the
888 three biomes that were well constrained by their in situ observation network, along with results
889 aggregated over the full continent; we show the approximate average of their "Simple" and
890 "NARR" inversions. The figure does not include a priori uncertainties for Gourджи et al. since
891 their method does not rely on a priori estimates. e) Fractional uncertainty reduction necessary to
892 meet the target requirement.

893 **Figure 11.** Ratio of the posterior uncertainty for the $2\times$ priors inversion to that for the standard
894 inversion, normalized by a factor of 2, for Case 1 in a) January, b) April, c) July, and d) October.

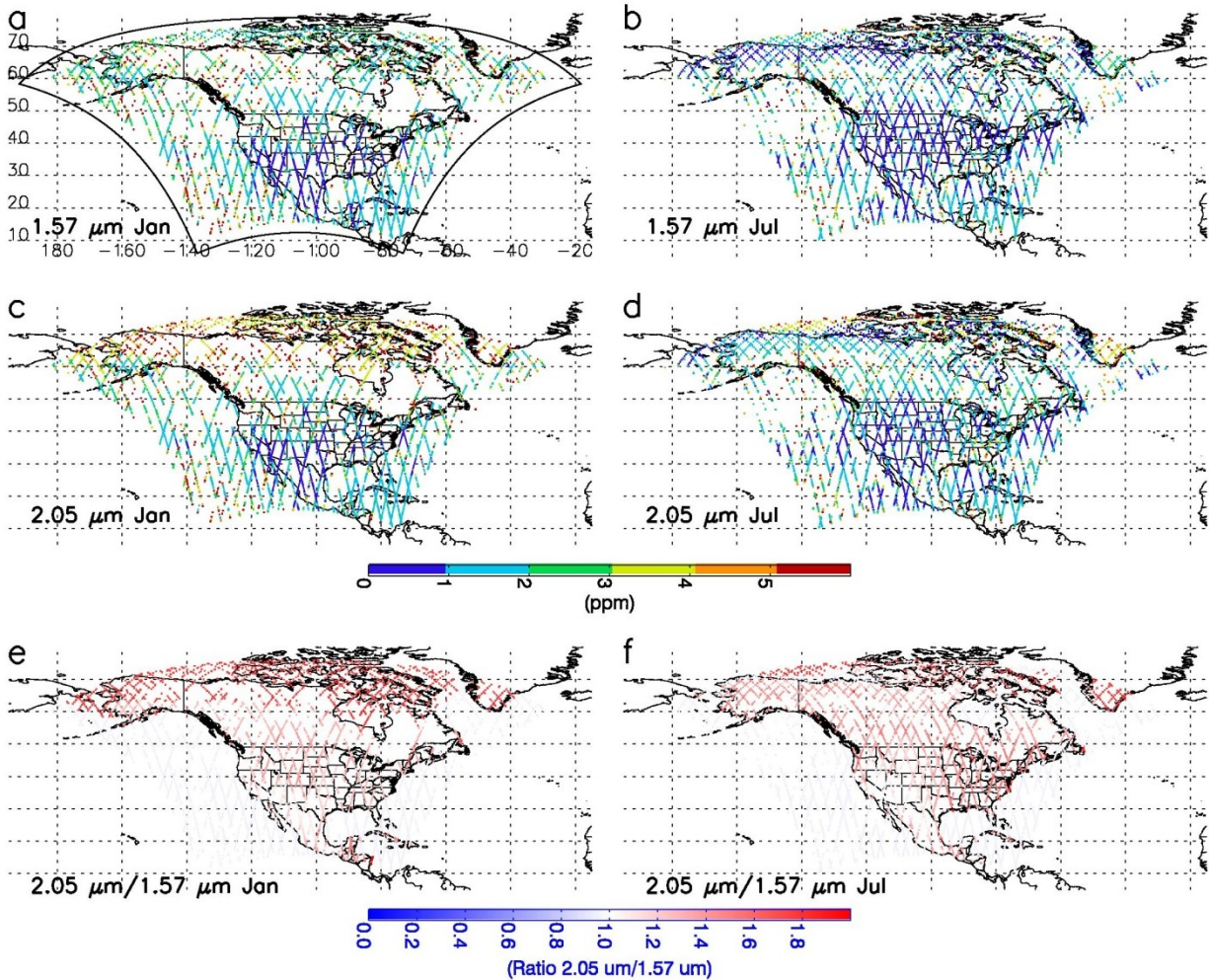
895



896

897 **Figure 1.** Vertical weighting functions per ppmv of CO₂ (10^{-6} ppmv⁻¹ hPa⁻¹) for two candidate
 898 ASCENDS wavelengths. These relate differential optical depth lidar measurements (on-line
 899 minus off-line) to column-average CO₂ mixing ratios. The precise on-line wavelengths used
 900 here are 1.571121 μm, which is 10 picometers (pm) offset from line center, and 2.051034 μm.

901

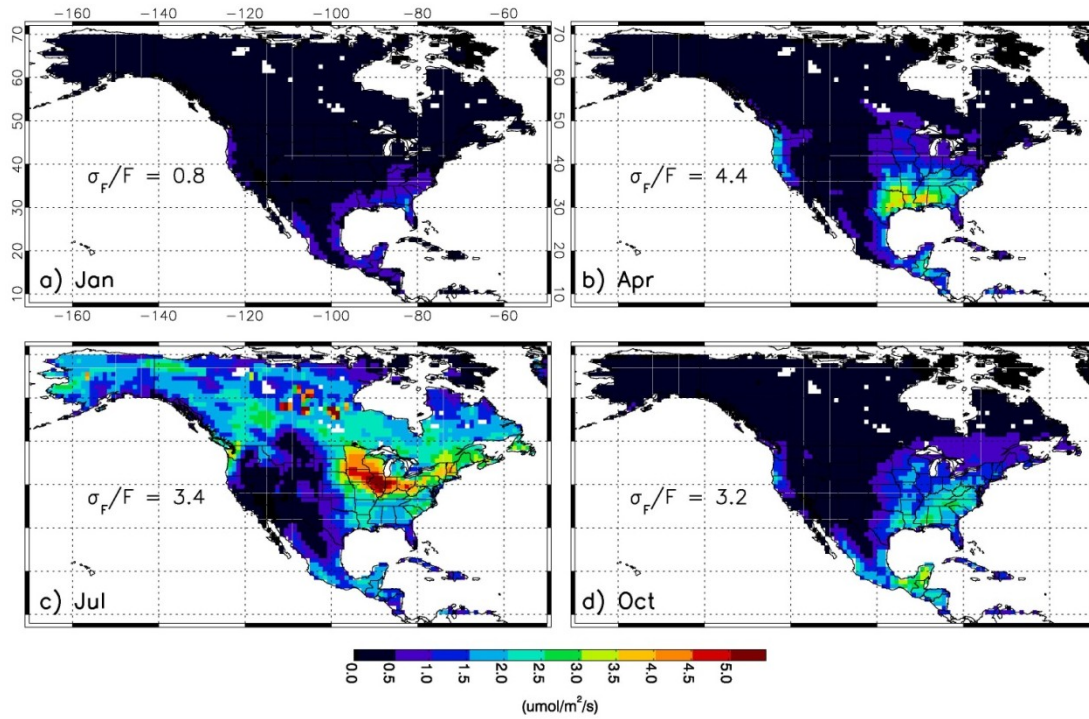


902

903 **Figure 2.** Examples of measurement locations (individual 10-s averages) and 10-s uncertainties
 904 (1σ) for the 0.5 ppm RRV random error case, across 7 day spans for a) the 1.57 μm wavelength
 905 in January and b) in July; and for c) the 2.05 μm wavelength in January and d) in July.

906 Locations with $\text{OD} > 0.7$ are rejected. e) Ratio of uncertainty for 2.05 μm to 1.57 μm in January
 907 and f) in July. The WRF domain for the runs utilized in this study is indicated by the bold, black
 908 lines in a).

909



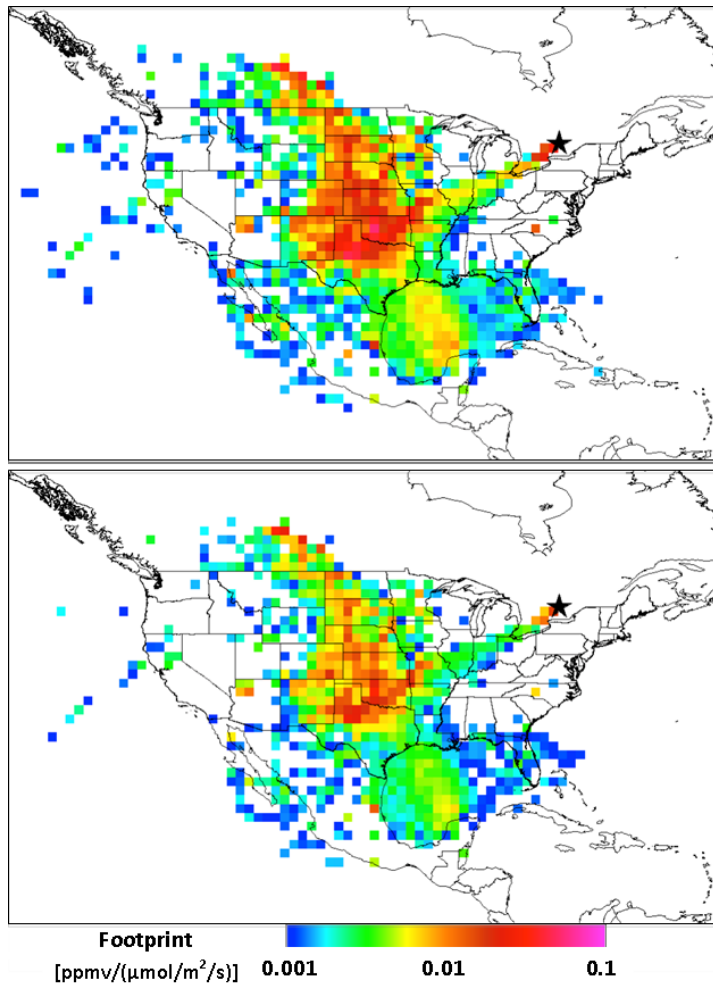
910

911 **Figure 3.** A priori weekly flux uncertainty for a) January, b) April, c) July, and d) October.

912 Average fractional flux uncertainties over the domain are given in each panel ($F \equiv \text{flux}$). $1 \mu\text{mol}$

913 $\text{m}^{-2} \text{s}^{-1} = 1.037 \text{ g C m}^{-2} \text{ d}^{-1} = 4.4 \times 10^{-8} \text{ kg CO}_2 \text{ m}^{-2} \text{ s}^{-1}$.

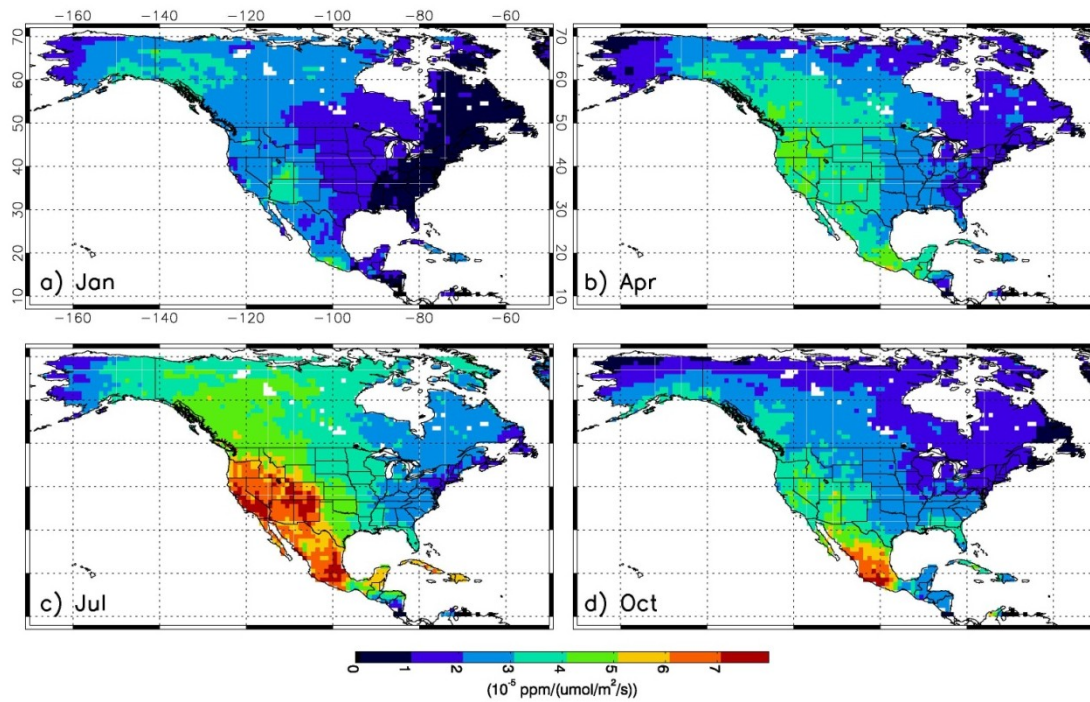
914



915

916 **Figure 4.** Footprint maps for one simulated ASCENDS measurement location (marked by black
 917 star) on January 1, 2007 at 18 UTC, integrated over 10 days and convolved over the 500-14500
 918 m AGL range with two candidate ASCENDS weighting functions: for the CO₂ laser lines at 2.05
 919 μm (top) and 1.57 μm (bottom). Units are ppm/($\mu\text{mol}/\text{m}^2/\text{s}$). Note that the native temporal
 920 resolution of the footprints is 3 hours; the 10-day integral in this figure is for illustrative purposes
 921 only. Only footprints over land are used in the analysis.

922

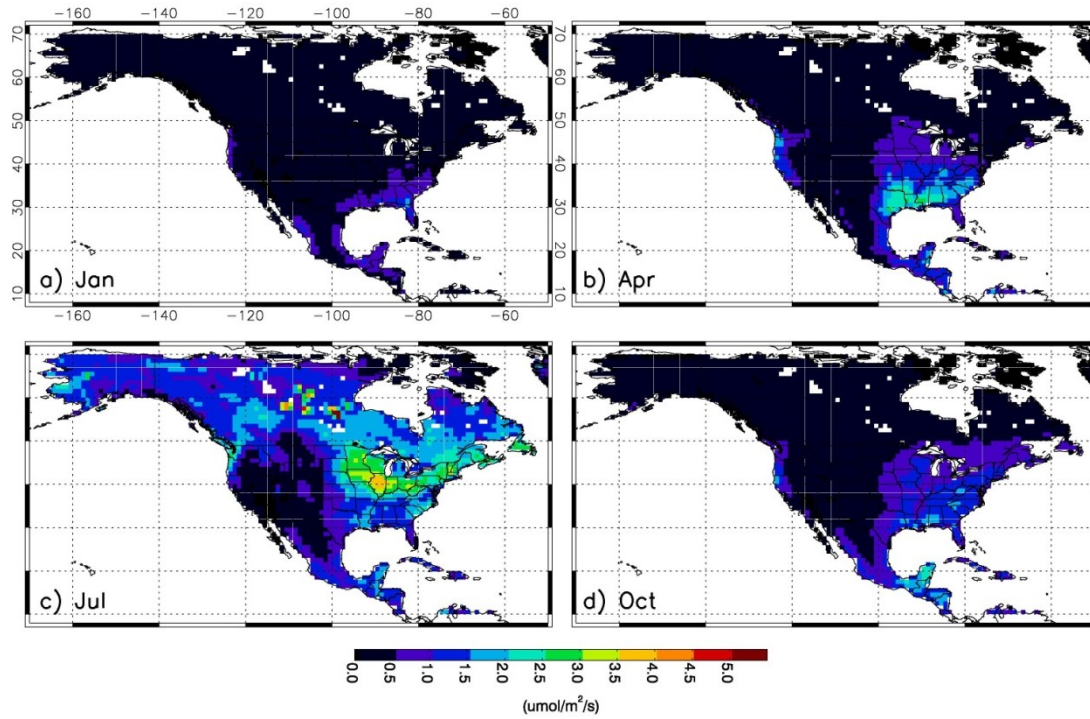


923

924 **Figure 5.** Jacobian values averaged over all observations and weekly flux intervals for a)

925 January, b) April, c) July, and d) October, for the 1.57 μm weighting function.

926



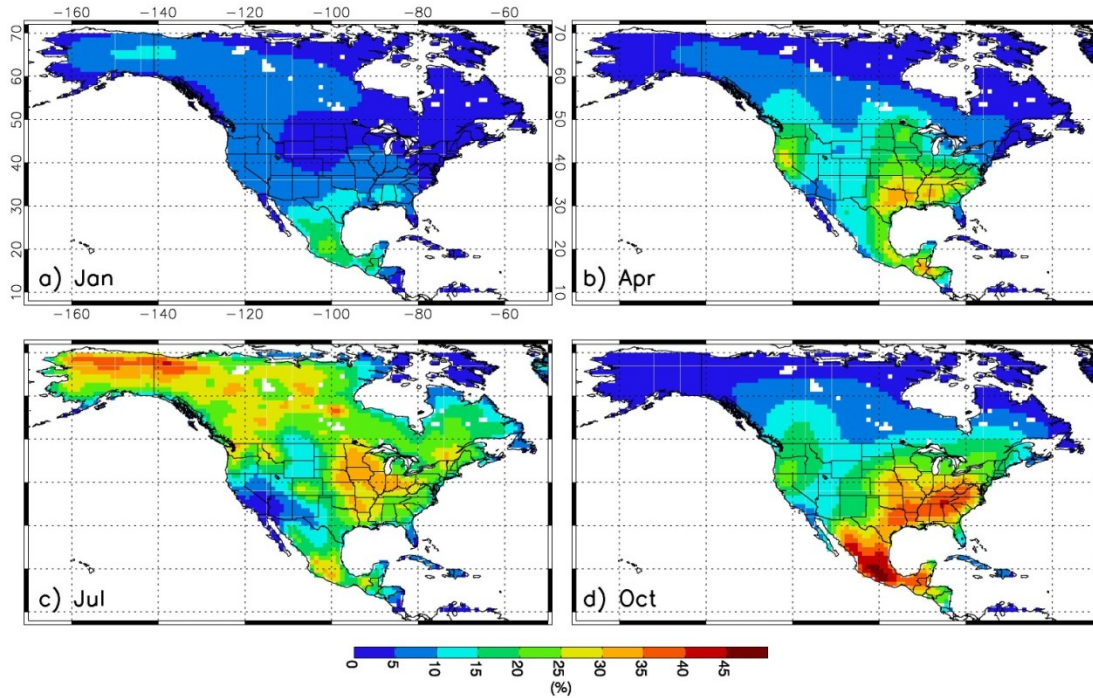
927

928 **Figure 6.** A posteriori weekly flux uncertainty over a) January, b) April, c) July, and d) October,

929 for Case 1 (1.57 μm and 0.5 ppm RRV error). Shown here are RMS values from the first 4

930 weeks of each month. $1 \mu\text{mol m}^{-2} \text{s}^{-1} = 1.037 \text{ g C m}^{-2} \text{ d}^{-1} = 4.4 \times 10^{-8} \text{ kg CO}_2 \text{ m}^{-2} \text{ s}^{-1}$.

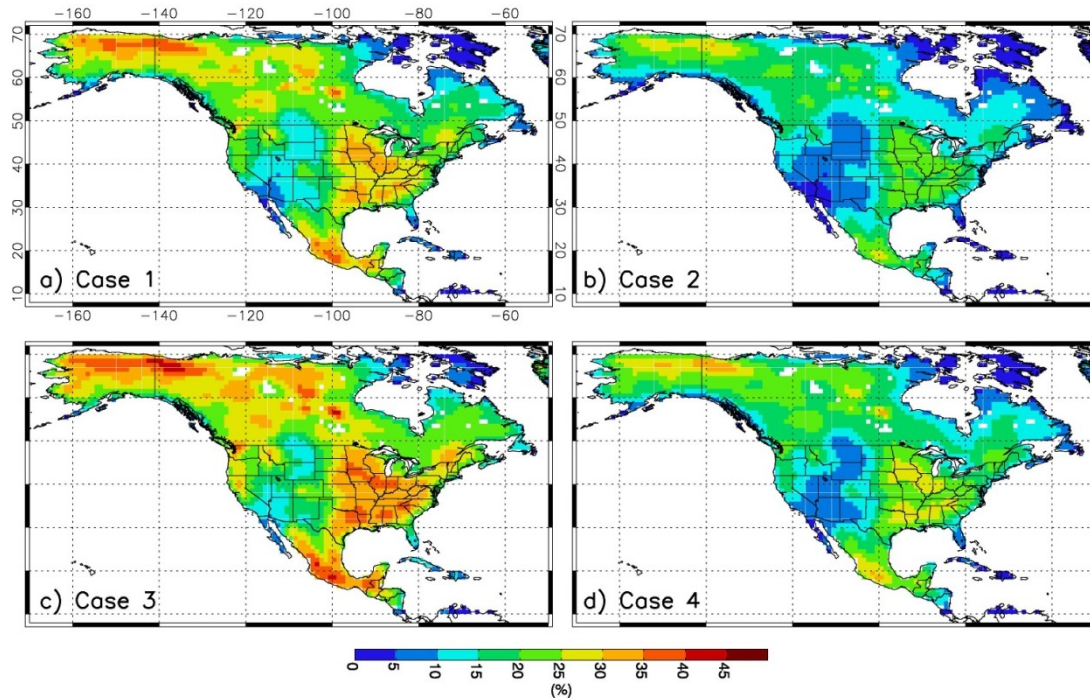
931



932

933 **Figure 7.** Weekly fractional flux uncertainty reduction over a) January, b) April, c) July, and d)
 934 October, for Case 1 ($1.57 \mu\text{m}$ and 0.5 ppm RRV error). Shown here are results from the first 4
 935 weeks of each month.

936



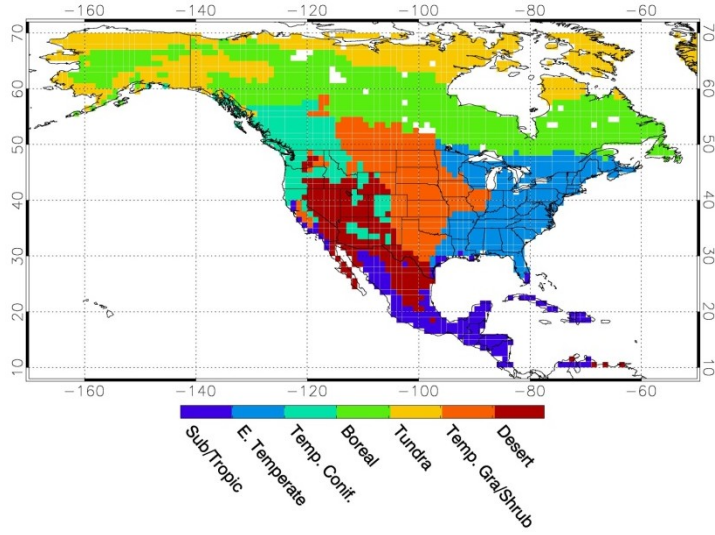
937

938 **Figure 8.** Weekly fractional flux uncertainty reduction (RMS over the 4 months) for a) Case 1

939 (1.57 μm and 0.5 ppm RRV error), b) Case 2 (1.57 μm and 1.0 ppm), c) Case 3 (2.05 μm and 0.5

940 ppm), and d) Case 4 (2.05 μm and 1.0 ppm).

941

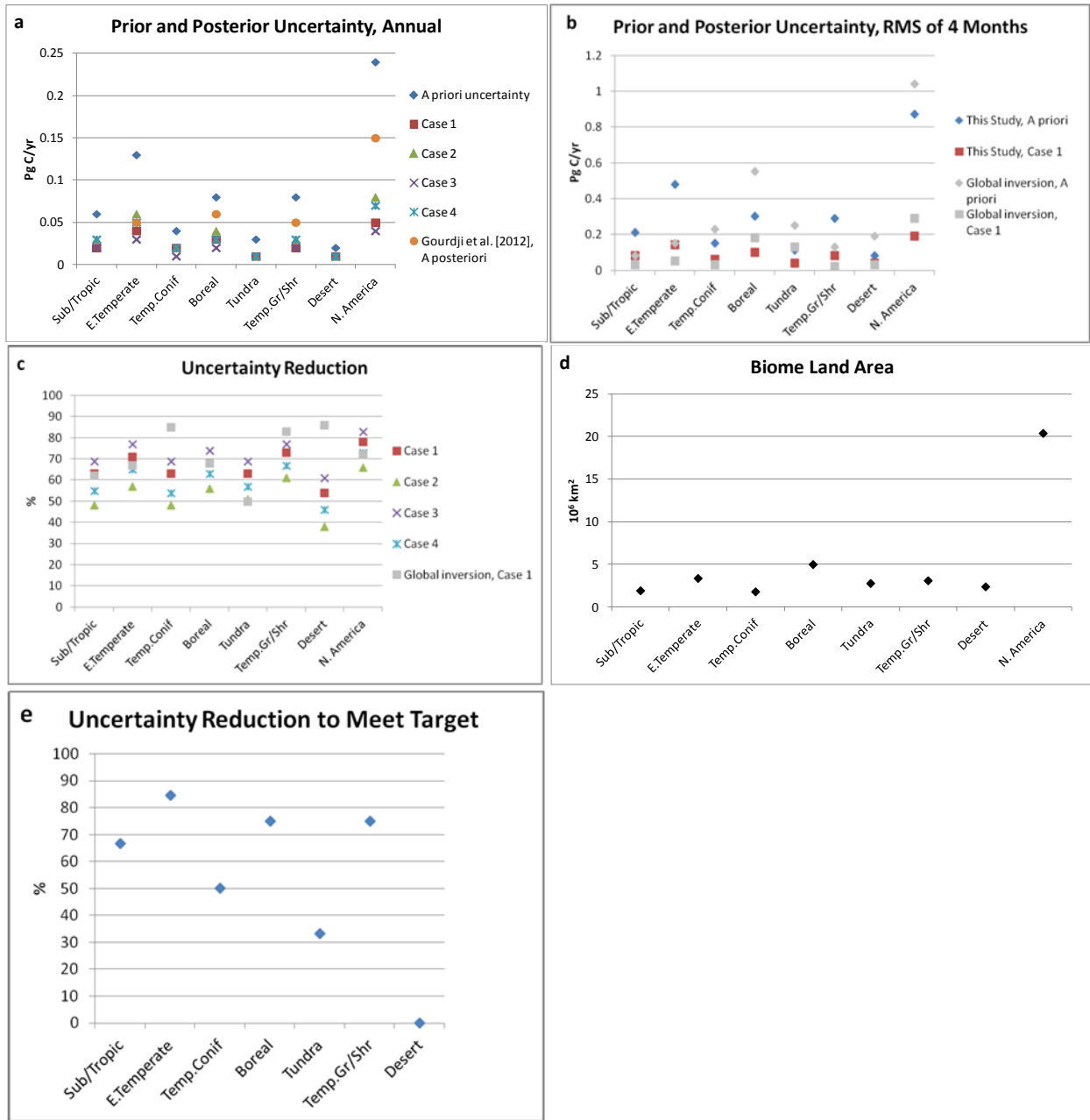


942

943 **Figure 9.** Biomes used, taken from Olson et al. [2001] with modifications by Gourджи et al.

944 [2012].

945

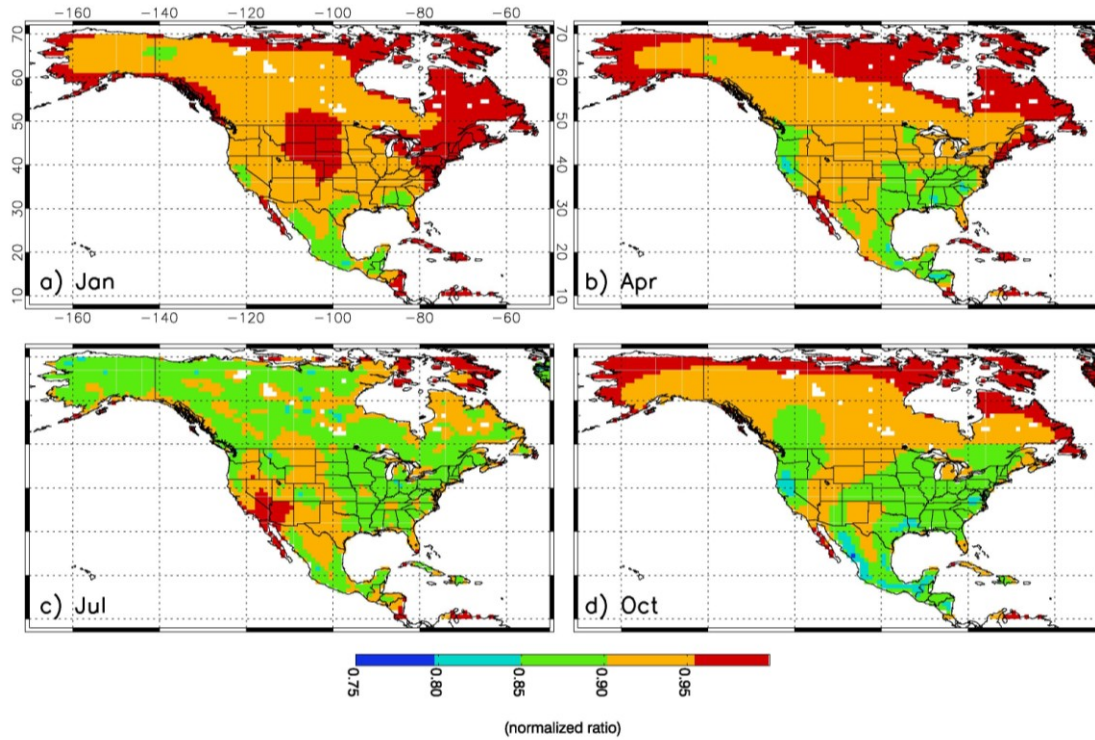


946

947 **Figure 10.** Results aggregated to biomes and continent, and compared with other studies. a) A
 948 priori and a posteriori uncertainties for the year, including results from Gourdji et al. [2012]. b)
 949 RMS of the four monthly uncertainties, including results from the global inversion. c) Fractional
 950 uncertainty reductions. d) Land area of the biomes. Gourdji et al. reported results for only the
 951 three biomes that were well constrained by their in situ observation network, along with results

952 aggregated over the full continent; we show the approximate average of their "Simple" and
953 "NARR" inversions. The figure does not include a priori uncertainties for Gourджи et al. since
954 their method does not rely on a priori estimates. e) Fractional uncertainty reduction necessary to
955 meet the target requirement.

956



957

958 **Figure 11.** Ratio of the posterior uncertainty for the $2\times$ priors inversion to that for the standard
 959 inversion, normalized by a factor of 2, for Case 1 in a) January, b) April, c) July, and d) October.

960